Fusion processes in collisions of ^{6}Li beams on heavy targets

J. Lubian,* J. L. Ferreira,† J. Rangel,‡ and M. R. Cortes§
Instituto de Física, Universidade Federal Fluminense, Avenida Litoranea s/n, Gragoatá, Niterói, RJ 24210-340, Brazil

L. F. Canto‖
Instituto de Física, Universidade Federal do Rio de Janeiro, CP 68528, Rio de Janeiro, RJ 21941-972, Brazil

(Received 17 November 2021; accepted 27 April 2022; published 5 May 2022)

We discuss a recently introduced model to evaluate complete and incomplete fusion in collisions of weakly bound nuclei. We propose a modification of the imaginary potential to deal with cross sections at energies well below the Coulomb barrier, and discuss the relation between the cross sections provided by a continuum discretized coupled-channel calculation and the ones measured in actual experiments. The new version of the model is used to make predictions of fusion cross sections in collisions of ^{6}Li with a few heavy targets, and the results are compared to the available data. The overall agreement between theory and experiment is quite good.

DOI: 10.1103/PhysRevC.105.054601

I. INTRODUCTION

Low-energy collisions of weakly bound nuclei have been attracting considerable interest in the last few decades [1–5]. In such collisions, breakup is a very important reaction mechanism, which has a large cross section and exerts strong influence on elastic scattering and typical nuclear reactions, like fusion, inelastic scattering, and particle transfer. Special attention has been given to the effect of the breakup channel on fusion [1,4–6] and reaction cross sections [7]. There are two main methods to assess this effect. The first is to compare experimental fusion cross sections to cross sections of calculations that neglect the breakup channels. The difference between these cross sections is then attributed to the breakup effect. The second method is to compare fusion data on weakly bound systems with data on tightly bound ones. In this case, it is necessary to eliminate trivial differences arising from system size and the height of the Coulomb barrier. This can be achieved by reducing the data, by the fusion function method [8,9] or another method available in the literature (see, e.g., Ref. [10]).

Owing to its low breakup threshold, a weakly bound projectile has a large probability of breaking up into two or more fragments, under the action of the combined Coulomb and nuclear fields of the target. This gives rise to different fusion processes. The first is the usual fusion of the whole projectile with the target, present also in collisions of tightly bound nuclei. This process is known as direct complete fusion (DCF). In addition, there are other fusion processes following breakup. In the case of projectiles that break up into two fragments, say c_1 and c_2, there are two incomplete fusion (ICF) processes. In the first ICF$_1$, fragment c_1 fuses with the target whereas c_2 emerges from the interaction region. In the second, ICF$_2$, the two fragments exchange their roles. Finally, there is the possibility that the two fragments fuse with the target sequentially. This process is called sequential complete fusion (SCF). DCF and SCF, which lead to the same compound nucleus (CN), cannot be distinguished experimentally. Only their sum, called complete fusion (CF), is an observable quantity. The sum of all fusion processes, namely, CF + ICF, is known as total fusion (TF).

Most of the fusion data available for weakly bound projectiles correspond to TF. Nevertheless, a few experiments involving some particular heavy target provide individual CF and ICF cross sections. These cross sections are available for collisions of ^{6}Li and/or ^{7}Li projectiles with ^{209}Bi [11,12], ^{159}Tb [13–15], ^{144,152}Sm [16–18], ^{165}Ho [19], ^{198}Pt [20,21], ^{154}Sm [22], ^{90}Zr [23], ^{124}Sn [24], and ^{197}Au [25] targets. Some data on the fusion of ^{9}Be with medium-heavy and heavy nuclei are also available [12,26–36]. As the present version of our model is limited to projectiles that break up into two fragments, and ^{9}Be breaks up into two alpha particles and a neutron, these collisions are not discussed here. In collisions of weakly bound projectiles with light- and intermediate-mass targets, the situation is much more complicated. In this case, the CNs produced in CF and ICF evaporate protons, so that the decay chains for the two fusion processes are intermixed. Then it is not possible to distinguish CF and ICF events.

Developing realistic theories to describe the fusion process in collisions of weakly bound nuclei is also a great challenge. The earliest theories to evaluate individual CF and ICF cross sections were based on classical [11,37–40] or semiclassical [41,42] physics. Thus, important quantum mechanical effects were not properly accounted for. Later, several quantum

*jlubian@id.uff.br
†jonas@if.uff.br
‡jeannierangel@gmail.com
§mariane.cortess@gmail.com
‖canto@if.ufrj.br

mechanical calculations based on the continuum discretized coupled-channel (CDCC) method were reported [43–51]. Some of them [43–45] could only evaluate the TF cross section, without determining the individual contributions from CF and ICF processes. This limitation was eliminated in the method of Refs. [46,47]. However, this method could not be applied to weakly bound nuclei that break up into fragments of comparable masses. More recently, Lei and Moro [52] and Parkar *et al.* [51] used indirect methods to determine cross sections for individual fusion processes. The former's authors obtained CF cross sections for the ^{6,7}Li + ^{209}Bi systems by subtracting from the total reaction (TR) cross sections the contributions of elastic breakup (EBU), inclusive nonelastic breakup (NEB), and inelastic scattering. The TR and the EBU cross sections were obtained through CDCC calculations, the NEB cross sections for the two fragments were obtained by the participant-spectator model of Ichimura *et al.* [53], and the inelastic scattering cross section was evaluated by standard coupled-channel calculations. In this way, they were able to reproduce fairly well the CF data on the two systems. Parkar *et al.* [51] used a different procedure. First, they performed three CDCC calculations using combinations of different short-range imaginary potentials. Then, comparing the absorption cross sections of these calculations, they determined the CF and ICF cross sections. Their method was applied to the ^{6,7}Li + ^{198}Pt and ^{209}Bi systems, and the results were shown to be in reasonable agreement with the data. There are also other promising models [50,54,55] that are not yet in the stage of making realistic predictions for fusion cross sections of weakly bound nuclei.

Very recently [48,49], we proposed a CDCC-based method to evaluate CF and ICF cross sections. This method was applied to collisions of ^{7}Li with a few heavy targets and the results were compared with the available data. The overall agreement between theory and experiment was very good, except at energies well below the Coulomb barrier, where the theoretical cross section overpredicted the data. Our calculations are consistent with the assumption that the breakup process is responsible for the suppression of CF, observed in collisions of weakly bound projectiles (see, e.g., Ref. [12]). On the other hand, this assumption is contradicted by other works [56,57], that conclude that the suppression mechanism is the direct stripping of a cluster. However, we believe that this disagreement is only apparent, as it results from the different treatments of the continuum in each work (this issue will be addressed in Sec. III A).

In the present paper, we introduce some refinements in the method of our previous works [48,49], and apply the improved version to collisions of ^{6}Li with some heavy targets. Particular attention is given to the CF cross sections at energies well below the Coulomb barrier, where our previous calculations overpredicted the data. As the breakup threshold of ^{6}Li is 1 MeV lower than that of ^{7}Li, the influence of the low binding energy on the fusion processes is expected to be more pronounced. The paper is organized as follows. In Sec. II, we introduce our theoretical model. We describe our CDCC calculations, and show how calculated fusion probabilities can be used to predict fusion cross sections of actual experiments. In Sec. III, we evaluate CF and ICF cross sections in collisions of ^{6}Li projectiles with ^{209}Bi, ^{197}Au, ^{124}Sn, and ^{198}Pt targets, and compare the predictions of our method with the available data. Finally, in Sec. IV, we present our conclusions and discuss future extensions of our method.

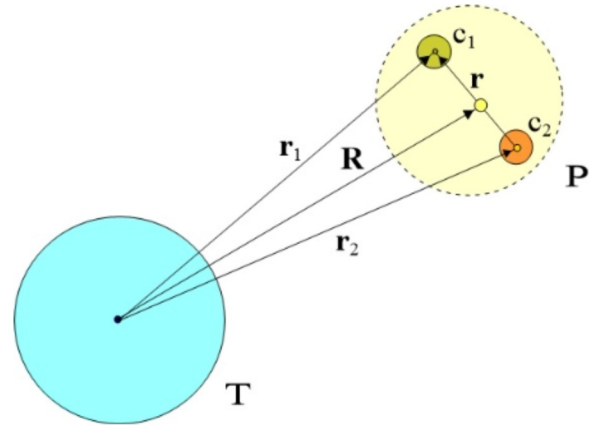

FIG. 1. Schematic representation of the vector coordinates in a collision of a projectile (P) composed of two clusters (c_1 and c_2) with a target (T).

II. THE THEORETICAL APPROACH

To calculate CF and ICF cross sections in collisions of ^{6}Li, we adopt the method of Refs. [48,49], with a slight modification [see the discussion after Eq. (31)]. The method describes fusion reactions in collisions of a projectile (P) with a target (T), assuming that the former is composed of two clusters, c_1 and c_2, which in the present case are, respectively, ^{2}H and ^{4}He. A description of the method is presented below.

Adopting a reference frame on the center of mass of the target, the reaction dynamics can be expressed in terms of two vector coordinates: the vector joining the centers of the two clusters, $\mathbf{r}$, and the one going from the center of mass of the target to that of the projectile, $\mathbf{R}$. Alternatively, one can use the position vectors of c_1 and c_2, $\mathbf{r}_1$ and $\mathbf{r}_2$. These coordinates are represented in Fig. 1. They are related to $\mathbf{r}$ and $\mathbf{R}$ by the equations

$$\mathbf{r}_1 = \mathbf{R} + \frac{A_2}{A_P}\,\mathbf{r}, \qquad \mathbf{r}_2 = \mathbf{R} - \frac{A_1}{A_P}\,\mathbf{r}. \tag{1}$$

Above, $A_1 = 2$ and $A_2 = 4$ are the mass numbers of the two clusters, and $A_P = 6$ is the mass number of the projectile. In the ground state of ^{6}Li, the clusters c_1 and c_2 are bound, with the separation energy (breakup threshold) $B = 1.47$ MeV.

The collision dynamics is determined by the full Hamiltonian of the system, given by

$$\mathbb{H}(\mathbf{R},\mathbf{r}) = h(\mathbf{r}) + \hat{T}_{\mathbf{R}} + \mathbb{V}(\mathbf{R},\mathbf{r}) - i\,\mathbb{W}(\mathbf{R},\mathbf{r}). \tag{2}$$

Above, $h(\mathbf{r})$ is the intrinsic Hamiltonian describing the motion of the clusters within the projectile, $\hat{T}_{\mathbf{R}}$ is the kinetic energy operator associated with the projectile-target relative motion, and $\mathbb{V}(\mathbf{R},\mathbf{r})$ is the real part of the interaction between the projectile and the target. Finally, $-\mathbb{W}(\mathbf{R},\mathbf{r})$ is the imaginary potential that accounts for the influence of the fusion channels, which are not explicitly included in channel expansion. One

should keep in mind that, to simulate the effects of fusion, the imaginary potential should be very strong and have a short range. That is, it must ensure total absorption in the inner region of the barrier, and be negligible elsewhere.

In the case of ^{6}Li, the intrinsic Hamiltonian has only one bound state, the ground state, ϕ_0. The remaining eigenstates of $h(\mathbf{r})$, ϕ_ε, are in the continuum (the breakup channels). They are labeled by the positive energy of the relative motion of the clusters (for simplicity, we omit other quantum numbers needed to specify the scattering states), ε. However, if one expands the full wave function over this set of states, one gets an infinite number of coupled equations. To avoid this problem, we use the CDCC approach [58,59], where the continuum is approximated by a set of N orthonormal wave packets (*bins*), ϕ_n ($n = 1, \ldots, N$). Then, the total wave function of the system, $\Psi^{(+)}(\mathbf{R}, \mathbf{r})$, can be written as

$$\Psi^{(+)}(\mathbf{R}, \mathbf{r}) = \Psi_0(\mathbf{R}, \mathbf{r}) + \Psi_{\rm BU}(\mathbf{R}, \mathbf{r}), \tag{3}$$

where

$$\Psi_0(\mathbf{R}, \mathbf{r}) = \psi_0(\mathbf{R}) \otimes \phi_0(\mathbf{r}) \tag{4}$$

is the wave function of the elastic channel, and

$$\Psi_{\rm BU}(\mathbf{R}, \mathbf{r}) = \sum_{n=1}^{N} \psi_n(\mathbf{R}) \otimes \phi_n(\mathbf{r}) \tag{5}$$

is the breakup wave function within the CDCC approximation.

Inserting Eqs. (3)–(5) into the full Schrödinger equation of the system, namely,

$$\mathbb{H}(\mathbf{R}, \mathbf{r})\ \Psi^{(+)}(\mathbf{R}, \mathbf{r}) = E\ \Psi^{(+)}(\mathbf{R}, \mathbf{r}),$$

and taking the scalar product with each of the intrinsic states, one gets the set of $N + 1$ coupled equations

$$[E - H_{00}(\mathbf{R})]\ \psi_0(\mathbf{R}) = \sum_{m=1}^{N} U_{0m}(\mathbf{R})\ \psi_m(\mathbf{R}) \tag{6}$$

and

$$[E_n - H_{nn}(\mathbf{R})]\ \psi_n(\mathbf{R}) = \sum_{m\neq n}^{N} U_{nm}(\mathbf{R})\ \psi_m(\mathbf{R}), \quad n = 1, \ldots, N. \tag{7}$$

Above, $E_n = E - \varepsilon_n$ is the relative energy in channel n and $U_{nm}(\mathbf{R})$ are the matrix elements of the total projectile-target interaction. These matrix elements are written as

$$U_{nm}(\mathbf{R}) = V_{nm}(\mathbf{R}) - i\, W_{nm}(\mathbf{R}), \tag{8}$$

with

$$V_{nm}(\mathbf{R}) = \int d^3\mathbf{r}\, \phi_n^*(\mathbf{r})\ \mathbb{V}(\mathbf{R}, \mathbf{r})\ \phi_m(\mathbf{r}), \tag{9}$$

$$W_{nm}(\mathbf{R}) = \int d^3\mathbf{r}\, \phi_n^*(\mathbf{r})\ \mathbb{W}(\mathbf{R}, \mathbf{r})\ \phi_m(\mathbf{r}). \tag{10}$$

The diagonal matrix elements, U_{nn}, play the role of *optical potentials* in the channel Hamiltonians,

$$H_{nn} = \hat{T}_{\mathbf{R}} + U_{nn}(\mathbf{R}),\ n = 0, \ldots, N, \tag{11}$$

TABLE I. Depth, radius, and diffusivity parameters of the volumetric (V_0, r_0, a_0) and spin-orbit ($V_0^{\rm SO}$, $r_0^{\rm SO}$, $a_0^{\rm SO}$) terms of $v_{12}(r)$ (taken from Ref. [44]). Energies are given in MeV and lengths are given in fm.

	V_0	r_0	a_0	$V_0^{\rm SO}$	$r_0^{\rm SO}$	$a_0^{\rm SO}$
^{6}Li (g.s.)	−78.46	1.15	0.7			
^{6}Li (res)	−80.0	1.15	0.7	2.5	1.15	0.7

whereas the off-diagonal matrix elements couple the elastic to the breakup channel, and also the breakup states among themselves.

The absorption cross section is given by the well-known expression [48,49,60]

$$\sigma_{\rm abs} = \frac{K}{E} \sum_{n,m=0}^{N} \langle \psi_n | W_{nm} | \psi_m \rangle, \tag{12}$$

where K is the wave number of the relative motion associated with the energy E. This expression plays a key role in calculations of fusion cross sections in collisions of weakly bound projectiles (see Sec. II B).

A. Nuclear interactions in the CDCC calculations

The theory of Refs. [48,49] is a three-body model, where the target and the two clusters forming the projectile are treated as structureless particles. Thus, the interactions between the two clusters, $v_{12}(r)$, between c_1 and the target, $\mathbb{V}^{1T}(r_1)$, and between c_2 and the target, $\mathbb{V}^{2T}(r_2)$, are essential ingredients of the model. These interactions are discussed below.

1. The intrinsic interaction and continuum discretization

The intrinsic Hamiltonian of Eq. (2) is

$$h(\mathbf{r}) = -\frac{\hbar^2}{2\mu_{12}}\nabla^2_{\mathbf{r}} + v_{12}(r), \tag{13}$$

where $\mu_{12} = m_0 A_1 A_2/(A_1 + A_2)$, with m_0 standing for the nucleon mass, is the reduced mass associated with the relative motion of the clusters within the projectile. The potential $v_{12}(r)$ is parametrized by a Woods-Saxon function, with parameters fitted to reproduce the binding energy of the ground state of ^{6}Li ($B = 1.47$ MeV), and its main resonances. In this procedure, it is necessary to use different parameters for the bound state and for the resonances. We adopt the parameters of Diaz-Torres *et al.* [44], which are listed in Table I. The experimental energies and widths of the main resonances of ^{6}Li are shown in Table II, in comparison with the energies and widths calculated with these potentials.

In our calculations, the interactions were expanded in multipoles, keeping multipolarities up to $\lambda_{\rm max} = 4$. The continuum discretized states (*bins*) were generated by scattering states of the two clusters, with orbital angular momenta up to $l_{\rm max} = 3\hbar$, and total angular momenta up to $j_{\rm max} = 4\hbar$. The discretization was performed in the energy space, taking into account the resonances of ^{6}Li. Finer meshes were used in the neighborhood of sharp resonances. We used the mesh represented in

TABLE II. Experimental and theoretical energies and widths of the main resonances of ^{6}Li (taken from Ref. [44]). The theoretical values were calculated with the parameters of the previous table.

l	j^π	$E_{\rm res}^{\rm th}$	$\Gamma_{\rm res}^{\rm th}$	$E_{\rm res}^{\rm exp}$	$\Gamma_{\rm res}^{\rm exp}$
2	3^+	0.717	0.020	0.716	0.024
2	2^+	3.14	1.88	2.84	1.7
2	1^+	4.06	3.5	4.18	1.5

Fig. 2. With this mesh and cutoff parameters ($\lambda_{\rm max}$, $j_{\rm max}$, and $l_{\rm max}$), we got very good convergence in all calculations in the present paper.

2. *The real projectile-target interaction*

The standard procedure in CDCC calculations is to write the real part of the projectile-target potential as a sum of interactions between the clusters c_1 and c_2 with the target. That is,

$$\mathbb{V}(\mathbf{R},\mathbf{r}) = \mathbb{V}^{(1T)}(\mathbf{r}_1) + \mathbb{V}^{(2T)}(\mathbf{r}_2). \tag{14}$$

The off-diagonal matrix elements of this potential couple the elastic channel to the continuum, and the continuum discretized states among themselves. On the other hand, its diagonal matrix elements are the real potentials in the channel Hamiltonians, on the left-hand side of Eqs. (6) and (7). In particular,

$$V_{00}(\mathbf{R}) = \int d^3\mathbf{r}\ |\phi_0(\mathbf{r})|^2\ [\mathbb{V}^{(1T)}(\mathbf{r}_1) + \mathbb{V}^{(2T)}(\mathbf{r}_2)], \tag{15}$$

where $\mathbf{r}_1$ and $\mathbf{r}_2$ are related with $\mathbf{R}$ and $\mathbf{r}$ by Eq. (1), is the real potential in the elastic channel, which determines the Coulomb barrier. Throughout the present paper, we adopt

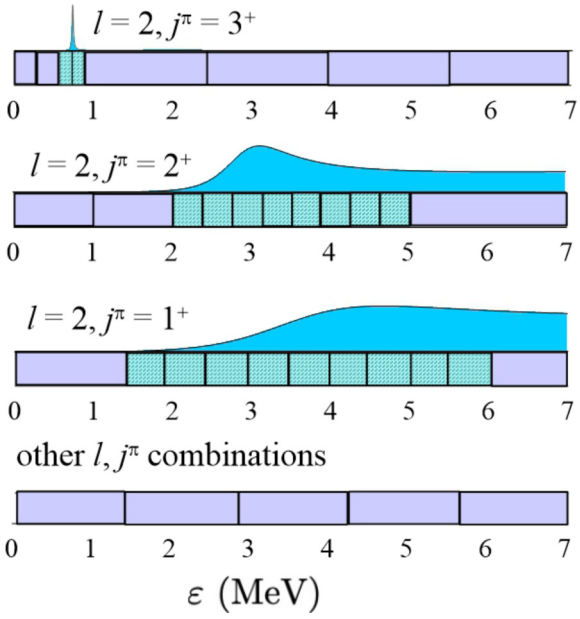

FIG. 2. Schematic representation of the discretization mesh used in our calculations. The resonances of Table II are also indicated (blue curves).

TABLE III. Barrier radii (R_B^{00}), curvature parameters ($\hbar\omega^{00}$), and heights (V_B^{00}) of $V_B^{00}(R)$ and barrier heights of $V_{PT}(R)$ ($V_B^{\rm PT0}$), for the ^{6}Li + ^{124}Sn, ^{6}Li + ^{197}Au, ^{6}Li + ^{198}Pt, and ^{6}Li + ^{209}Bi systems. The last line shows the reduction of the barrier height due to the low breakup threshold of ^{6}Li.

Target	^{124}Sn	^{197}Au	^{198}Pt	^{209}Bi
R_B^{00} (fm)	10.8	11.6	11.7	11.7
$\hbar\omega^{00}$ (fm)	3.6	4.2	4.2	4.3
V_B^{00} (MeV)	18.4	27.1	26.7	28.2
V_B^{PT} (MeV)	19.7	28.8	28.4	29.9
ΔV_B (MeV)	1.3	1.7	1.7	1.7

the São Paulo potential [61,62] (SPP) for the real part of the nuclear interactions between the clusters and the target. For the Coulomb interaction, we adopt the usual procedure in nucleus-nucleus collisions, used, for example, in Refs. [48,49].

Owing to the low breakup threshold of the projectile, the wave function ϕ_0 has a long tail. For this reason, the barriers of $V_{00}(R)$, denoted by V_B^{00}, are systematically lower than those of the SPP between the projectile and the target, neglecting the cluster structure. The latter potential and its Coulomb barrier are denoted by $V_{PT}(R)$ and V_B^{PT}, respectively. The barrier lowering effect arising from the low breakup threshold is illustrated in Table III, for several targets. It shows V_B^{00}, V_B^{PT}, and the reduction of the barrier height due to the cluster structure of the projectile (the *static effect* of the low breakup threshold), ΔV_B. For the three heaviest targets, which are very similar, one finds $\Delta V_B = 1.7$ MeV. For the lighter ^{124}Sn target, the reduction is 0.4 MeV lower. The table shows also the radius and curvature parameters of the parabolic expansion of $V_{00}(R)$, denoted by R_B^{00} and $\hbar\omega^{00}$.

The influence of the barrier lowering on fusion is illustrated in Table IV, where we show fusion cross sections of one-channel calculations with the two real potentials, with short-range absorption. In both calculations, the imaginary potential is represented by a negative Woods-Saxon function with strength $W_0 = 50$ MeV, radius parameter $r_w = 1.0$ fm, and diffusivity $a_w = 0.2$ fm. The targets are the same of the previous table. In each case, the cross sections are calculated at the collision energy $E_{\rm c.m.} = V_B^{00} + 10$ MeV. One concludes that the reduction of the Coulomb barrier enhances the fusion cross sections by ≈30%.

a. Bound-continuum couplings. The continuum discretized bins, $|\phi_n)$, are linear combinations of scattering states of the clusters c_1 and c_2. However, the cluster state $|\phi_0)$ is just an

TABLE IV. Cross sections of one-channel calculations with V_{00} (σ_{00}) and V_{PT} (σ_{PT}). For each system, the cross section is evaluated at the collision energy $E_{\rm c.m.} = V_B^{00} + 10$ MeV.

Target	^{124}Sn	^{197}Au	^{198}Pt	^{209}Bi
σ_{00} (mb)	1244	1094	1106	1136
σ_{PT} (mb)	964	815	931	830
σ_{00}/σ_{PT}	1.3	1.3	1.2	1.4

approximation for the actual ground state of ^{6}Li, $|\phi_{\text{g.s.}}\rangle$. One can write

$$|\phi_{\text{g.s.}}\rangle = \alpha\,|\phi_0\rangle + \beta|\phi_\perp\rangle \text{ (with } \alpha^2+\beta^2=1), \quad (16)$$

where $|\phi_\perp\rangle$ is a state orthogonal to $|\phi_0\rangle$, which does not have the cluster structure. Thus, matrix elements of the coupling interaction between $|\phi_\perp\rangle$ and $|\phi_n\rangle$ vanish. Although $|\phi_0\rangle$ is close to $|\phi_{\text{g.s.}}\rangle$, the coefficient α is not exactly equal to 1. This statement is supported by the fact that large cross sections for one-nucleon transfer reactions have been observed in collisions of ^{6}Li with different targets [63–66]. Thus, this coefficient must be somewhat lower than 1. We point out that spectroscopic amplitudes are also used in calculations of transfer cross sections [67–70], and a similar procedure is adopted in cluster decays of a heavy nucleus. In the latter case, it appears as a preformation probability in calculations of half-lives (see, e.g., Refs. [71,72]).

Surely, setting $\alpha = 1$ is a reasonable approximation, at least for a qualitative calculation. However, if one aims at obtaining accurate descriptions of data, one should allow for smaller values of α. In this case, matrix elements of the coupling interaction between the elastic channel and bins ($n \neq 0$) should be written

$$V_{0n}(\mathbf{R}) = \alpha\,\langle\phi_0|\,\mathbb{V}\,|\phi_n\rangle, \quad (17)$$

$$V_{n0}(\mathbf{R}) = \alpha\,\langle\phi_n|\,\mathbb{V}\,|\phi_0\rangle. \quad (18)$$

For simplicity, we are assuming that the spectroscopic amplitude, α, is real. Since the precise value of α is unknown, we treat it as an adjustable parameter of the order of 1, varying within the interval $1 \geqslant \alpha \geqslant 0.5$.

3. The imaginary potential

Different imaginary potentials have been used in CDCC calculations of fusion cross sections. Hagino *et al.* [46] and Diaz-Torres and Thompson [47] adopted a strong absorption potential with a short range, depending exclusively on the projectile-target distance, R. It was parametrized by the Woods-Saxon (WS) function:

$$\mathbb{W}_{PT}(R) = \frac{W_0}{1+\exp\left[(R-R_w)/a_w\right]}, \quad (19)$$

where $R_w = r_w\,[A_P^{1/3} + A_T^{1/3}]$, with the parameters $W_0 = 50$ MeV, $r_w = 1.0$ fm, and $a_w = 0.1$ fm.

Other CDCC calculations [44,48,49,51] used the sum of short-range imaginary potentials:

$$\mathbb{W}(\mathbf{R},\mathbf{r}) = \mathbb{W}^{(1)}(r_1) + \mathbb{W}^{(2)}(r_2), \quad (20)$$

where $\mathbb{W}^{(1)}(r_1)$ and $\mathbb{W}^{(2)}(r_2)$ absorb the clusters c_1 and c_2, respectively. These potentials were parametrized by the WS functions:

$$\mathbb{W}^{(i)}(r_i) = \frac{W_0}{1+\exp[(r_i - R_w^{(i)})/a_w]}, \qquad i = 1, 2, \quad (21)$$

with $W_0 = 50$ MeV, $R_w^{(i)} = r_w\,[A_i^{1/3} + A_T^{1/3}]$, with short-range radius and diffusivity parameters ($r_w = 1.0$ fm, $a_w = 0.1$ fm). The potential of Eq. (20) has the advantage of allowing for the absorption of each cluster, individually, which is suitable for calculations of separate cross sections for the different fusion processes. Note that this imaginary potential is not diagonal in channel space. Its diagonal matrix element for the ground state of ^{6}Li,

$$W_{00}(R) = \int d^3\mathbf{r}\,|\phi_0(\mathbf{r})|^2\,[\mathbb{W}^{(1)}(\mathbf{R},\mathbf{r}) + \mathbb{W}^{(2)}(\mathbf{R},\mathbf{r})], \quad (22)$$

plays the role of the imaginary part of the optical potential in the elastic channel.

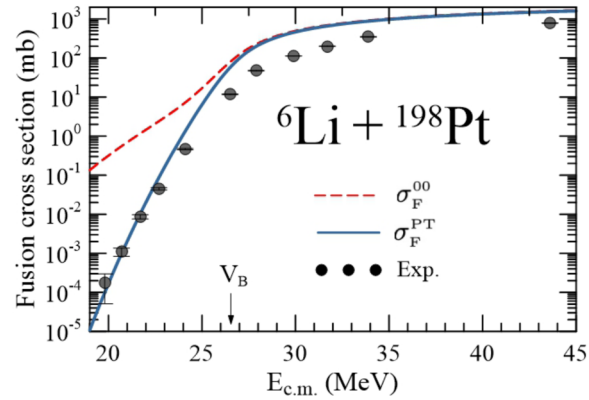

FIG. 3. Fusion excitation functions for the ^{6}Li + ^{198}Pt system obtained by one-channel calculations using the potentials $V_{00} - iW_{PT}$ and $V_{00} - iW_{00}$. For comparison, the data of Shrivastava *et al.* [20] are also shown.

The imaginary potential of Eqs. (20) and (21) was used to evaluate CF and ICF cross sections in collisions of ^{7}Li with several targets, and the results were compared to the available data [49]. The overall agreement between theory and experiment was quite good. However, the theoretical CF cross sections became much larger than the data at energies well below the Coulomb barrier ($E_{\text{c.m.}} \lesssim V_B^{00} - 4$ MeV). This shortcoming was traced back to the long tail of the imaginary potential of Eq. (22), resulting from the extended range of ϕ_0. This tail gives rise to absorption around the barrier radius and beyond, which cannot be associated with fusion. In collisions of ^{6}Li, the situation is expected to be much worse. Owing to the lower breakup threshold of ^{6}Li, ϕ_0 has a much longer tail, so that $W_{00}(R)$ reaches far beyond the barrier radius. Then, at energies well below the Coulomb barrier, where the classical turning point is much larger than the barrier radius, σ_{abs} is dominated by absorption outside the Coulomb barrier. Since the imaginary potential is meant to account for fusion, the cross section calculated with the imaginary potential of Eq. (22) is not reliable in this energy region. A quantitative discussion of this problem is presented below.

At energies well below the Coulomb barrier, σ_{SCF} is much smaller than σ_{DCF}. In this way, the CF cross section reduces to the much simpler cross section of a one-channel calculation with the potential $U(R) = V_{00}(R) - i\,W_{00}(R)$. This has been explicitly shown in the case of ^{7}Li projectiles (see the logarithmic plots in Figs. 8–11 of Ref. [49]). The consequence of the spurious behavior of W_{00} at long distances is illustrated in Fig. 3. It shows fusion excitation functions for the ^{6}Li + ^{198}Pt system, obtained by one-channel calculations with the complex potentials $V_{00} - iW_{00}$ and $V_{00} - iW_{PT}$, where W_{PT}

is the imaginary potential of Eq. (19). The cross sections for these potentials are denoted by σ_F^{00} (red dashed line) and σ_F^{PT} (solid blue line), respectively. Above the Coulomb barrier, the fusion cross sections of the two one-channel calculations are extremely close. Further, one notices that the CF data are appreciably lower than the results of the two calculations in this energy range, exhibiting the above-barrier suppression, extensively discussed in the literature (see, e.g., Ref. [4]). The situation is completely different at energies well below the Coulomb barrier. In this region, σ_F^{PT} converges to the CF data, whereas σ_F^{00} is a few orders of magnitude larger.

The origin of the unrealistically large values of σ_F^{00} at energies well below the Coulomb barrier may be traced back to long-range absorption. To prove it, we resort to the partial-wave projected version of Eq. (12). In one-channel calculations the sum over channels reduces to the contribution from the elastic channel ($n = m = 0$), and one can write [60]

$$\sigma_{\rm abs} = \sum_J \sigma(J), \quad \text{with} \quad \sigma(J) = \frac{\pi}{K^2}\,(2J+1)\,\mathcal{P}(J), \qquad (23)$$

where K is the wave number and $\mathcal{P}(J)$ is the absorption probability in a collision with angular momentum J. It is given by

$$\mathcal{P}(J) = \frac{4K}{E}\int dr\, W(R)\,|u_{0J}(R)|^2, \qquad (24)$$

where $u_{0J}(R)$ is the corresponding radial wave function and $W(R)$ is the modulus of the imaginary potential.

To determine the region in the R space that gives dominant contributions to the absorption probabilities, we inspect the integrand of Eq. (24) for the imaginary potentials, $W(R) = W_{00}(R)$ and $W_{PT}(R)$. These integrands are denoted by $I_{00}(R)$ and $I_{PT}(R)$, respectively. We consider two collision energies: $E_{\rm c.m.} = 19.8$ MeV (≈9 MeV below the barrier) and $E_{\rm c.m.} = 43.6$ MeV (≈15 MeV above the barrier). In each case, the integrand is evaluated at the angular momentum that gives the largest contribution to the absorption cross section, namely, $J = 3\hbar$ for $E_{\rm c.m.} = 19.8$ MeV, and $J = 22\hbar$ for $E_{\rm c.m.} = 43.6$ MeV. These integrands are shown in Fig. 4. To help the comparison between $I_{00}(R)$ and $I_{PT}(R)$, which may have different orders of magnitude, they are renormalized as to have maxima equal to 1.

For the above-barrier energy [Fig. 4(a)], $I_{00}(R)$ and $I_{PT}(R)$ have different shapes, but they share the common feature of being concentrated within the inner region of the barrier. The broader shape of $I_{00}(R)$ results from the slowly decreasing tail of $W_{00}(R)$. On the other hand, the fast decreasing tail of $W_{PT}(R)$ leads to a sharp peak in $I_{PT}(R)$. Note that the small width of this peak is compensated by its larger maximum (it cannot be seen in the figure because the two curves are renormalized), so that the two integrals are very close. This has a simple physical interpretation. At energies well above the barrier, the incident wave is fully transmitted through the barrier and completely absorbed by any of the two imaginary potentials. Then, the cross sections σ_F^{00} and σ_F^{PT} are very close. The situation is quite different at $E_{\rm c.m.} = 19.8$ MeV [Fig. 4(b)]. $I_{PT}(R)$ remains concentrated within the inner region of the barrier, whereas $I_{00}(R)$ is negligible there. It is relevant only at large distances, beyond the radius of the Coulomb barrier. Therefore, the resulting absorption probability cannot be associated with any fusion process.

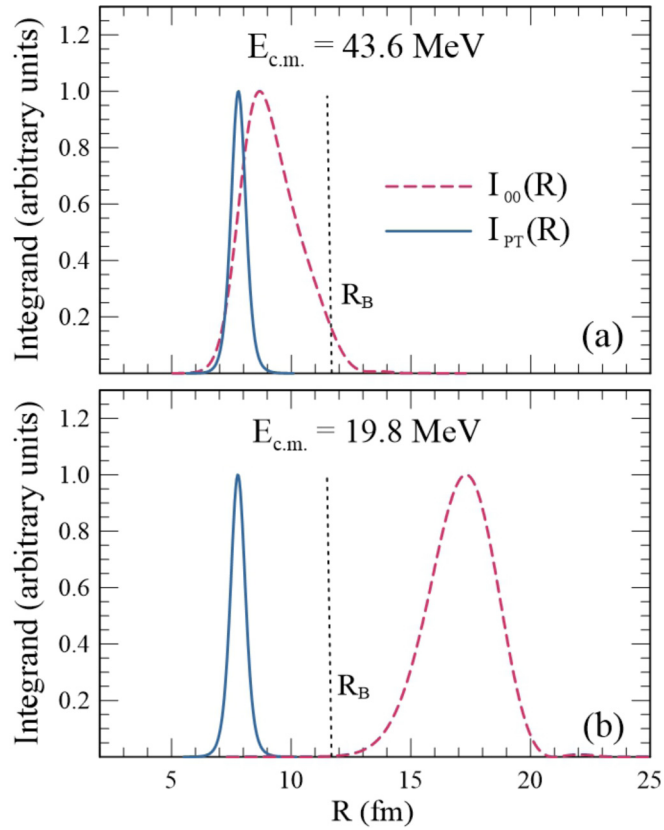

FIG. 4. The integrands $I_{PT}(J)$ and $I_{00}(J)$ for the ^{6}Li + ^{198}Pt system, for the collision energies (a) $E_{\rm c.m.} = 19.8$ MeV and (b) $E_{\rm c.m.} = 43.6$ MeV. They are evaluated at the angular momenta $J = 3\hbar$ and $22\hbar$, respectively. See the text for details.

In summary, the imaginary potential $\mathbb{W} = \mathbb{W}^{(1)} + \mathbb{W}^{(2)}$ [Eq. (20)] is essential for a proper calculation of the contributions from the unbound channels to the different fusion processes. However, it leads to very wrong CF cross sections at sub-barrier energies. On the other hand, the potential $\mathbb{W}_{PT}$ of Eq. (19) describes very well the CF cross sections in this energy region, but it cannot account for the fusion of a single fragment.

In the present paper we adopt phenomenological imaginary potentials for the bound and unbound spaces satisfying two conditions. The first is that of being strong enough to absorb completely the incoming current that overcomes the barrier of the potential between the fusing partners, that is, the projectile-target potential in the case of DCF, and the fragment-target potentials, in the cases of ICF and SCF. The second condition is that of being negligible around and beyond the barrier radius. To satisfy these conditions, we adopt the following procedures.

(1) We use the imaginary potential $\mathbb{W}_{PT}$ to evaluate matrix elements of the imaginary potential between bound channels.

(2) We use the imaginary potential $\mathbb{W} = \mathbb{W}^{(1)} + \mathbb{W}^{(2)}$ to evaluate matrix elements of the imaginary potential between CDCC bins.

(3) As in Refs. [48,49], we neglect matrix elements of the imaginary potential between bound and unbound channels.

Formally, the complex potential acting on the elastic channel in a one-channel calculation can be derived by Feshbach's formalism [73]. One introduces a projector onto the elastic channel, $\mathcal{P}$, and a projector onto a set of channels that have strong influence on elastic scattering, $\mathcal{Q}$. Then, the effective potential acting on the elastic channel is given by

$$\mathbb{U}_{\text{eff}} = \mathcal{P}\,\mathbb{U}\,\mathcal{P} + \mathcal{P}\,\mathbb{U}\,\mathcal{Q}\,[\mathbb{G}_{\mathcal{Q}\mathcal{Q}}]\,\mathcal{Q}\,\mathbb{U}\,\mathcal{P}, \tag{25}$$

where $\mathbb{G}_{\mathcal{Q}\mathcal{Q}}$ is the Green's function in the $\mathcal{Q}$ subspace. The first term in the above equation is the potential in the elastic channel when all couplings are neglected, and the second is a polarization potential accounting for the influence of nonelastic channels on elastic scattering. This procedure has been used to derive complex polarization potentials associated with different direct reactions (a recent review can be found in Ref. [74]).

The above procedure can be extended to coupled-channel descriptions of heavy ion scattering. In this case, the elastic channel and a set of nonelastic channels are taken into account explicitly, whereas other channels are left out of the coupled equations. In our CDCC calculations, the bound channels (B) and the continuum discretized channels (C) are explicitly included in the calculations, and they are associated with projectors $\mathcal{P}_B$ and $\mathcal{P}_C$, respectively. On the other hand, there are important channels that have been left out of the coupled equations, namely, CF, ICF1, and ICF2, together with all intermediate channels populated in the thermalization processes. These channels are associated with a projector $\mathcal{Q}$. The imaginary parts of the polarization potentials acting on the B and C spaces are then given by

$$\begin{aligned}\mathbb{W}_B &= \text{Im}\{\mathcal{P}_B\,\mathbb{U}\,\mathcal{Q}\,[\mathbb{G}_{\mathcal{Q}\mathcal{Q}}]\mathcal{Q}\,\mathbb{U}\,\mathcal{P}_B\},\\ \mathbb{W}_C &= \text{Im}\{\mathcal{P}_C\,\mathbb{U}\,\mathcal{Q}\,[\mathbb{G}_{\mathcal{Q}\mathcal{Q}}]\,\mathcal{Q}\,\mathbb{U}\,\mathcal{P}_C\}.\end{aligned} \tag{26}$$

However, the above equations are not very useful because the projector $\mathcal{Q}$ involves many intrinsic degrees of freedom, and it is defined in a space of extremely large dimension. Thus, its calculation is prohibitively complicated, even within approximations. For this reason, practical one-channel and coupled-channel calculations of fusion cross sections adopt phenomenological imaginary potentials consistent with the nature of the fusion processes and the main trends of the data.

B. CF, ICF, and TF cross sections

The CDCC calculation leads to the following cross sections:

$$\sigma_{\text{DCF}} = \frac{\pi}{K^2}\sum_J (2J+1)\,\mathcal{P}^{\text{DCF}}(J), \tag{27}$$

$$\sigma_F^{(1)} = \frac{\pi}{K^2}\sum_J (2J+1)\,\mathcal{P}^{(1)}(J), \tag{28}$$

$$\sigma_F^{(2)} = \frac{\pi}{K^2}\sum_J (2J+1)\,\mathcal{P}^{(2)}(J). \tag{29}$$

Above, $\mathcal{P}^{\text{DCF}}$ is the probability of direct absorption of the whole projectile by the target. It results from the action of $\mathbb{W}_{PT}$ on bound channels (only the elastic channel in collisions of ^{6}Li). On the other hand, $\mathcal{P}^{(i)}$ is the probability of absorption of fragment c_i, following breakup. It results from the action of $\mathbb{W}^{(i)}$ on unbound channels. These probabilities are discussed in the appendices of Ref. [49].

However, the above cross sections are not the ones determined in experiments. First, σ_{DCF} is the cross section for direct complete fusion, whereas an experiment can only measure σ_{CF}, which includes also the contribution from SCF. Besides, $\sigma_F^{(1)}$ and $\sigma_F^{(2)}$ are inclusive cross sections for the capture of one of the fragments, independently of what happens to the other. In this way, SCF is included in both $\sigma_F^{(1)}$ and $\sigma_F^{(2)}$. Thus, the sum $\sigma_F^{(1)} + \sigma_F^{(2)}$, which is frequently assumed to give σ_{TF} (see, e.g., Refs. [48,49]), is in fact an overestimate of this cross section, where the contribution of SCF is counted twice.

The fact that a CDCC calculation is unable to account for sequential fusion processes is not surprising. Multistep processes are properly handled in coupled-channel calculations when all intermediate states are included in channel space, and their coupling matrix elements are taken into account. However, these conditions are not satisfied by SCF. In this case, neither the intermediate state after the capture of the first fragment nor the final state after the capture of the second is explicitly included in the calculations. The simulation of fusion by imaginary potentials can account for the depletion of flux in each channel, but it cannot describe the sequential fusion of two fragments. Thus, the CDCC approach alone cannot describe the SCF and ICF processes. Therefore, it is necessary to introduce some model to relate $\mathcal{P}^{(1)}(J)$ and $\mathcal{P}^{(2)}(J)$ to ICF and SCF probabilities. We adopt the model of Refs. [48,49], with a slight modification, as described below.

We treat $\mathcal{P}^{(1)}(J)$ and $\mathcal{P}^{(2)}(J)$ as probabilities for independent events, and use classical statistics. The ICF1, ICF2, and SCF probabilities are assumed to be given by

$$\mathcal{P}^{\text{ICF1}}(J) = \mathcal{P}^{(1)}(J) \times [1 - \mathcal{P}^{(2)}(J)], \tag{30}$$

$$\mathcal{P}^{\text{ICF2}}(J) = \mathcal{P}^{(2)}(J) \times [1 - \mathcal{P}^{(1)}(J)], \tag{31}$$

$$\mathcal{P}^{\text{SCF}}(J) = \mathcal{P}^{(1)}(J) \times \mathcal{P}^{(2)}(J). \tag{32}$$

Note that Eq. (32) does not have the factor 2 appearing in the SCF probability of Refs. [42,48,49]. The discrepancy arises from the different expressions adopted for the TF probability. In these works, it is given by

$$\mathcal{P}^{\text{TF}}(J) = \mathcal{P}^{\text{DCF}}(J) + \mathcal{P}_C^{\text{TF}}(J), \tag{33}$$

where $\mathcal{P}_C^{\text{TF}}$ represents the sum of all fusion processes following breakup (contribution from bin states to fusion):

$$\mathcal{P}_C^{\text{TF}}(J) = \mathcal{P}^{(1)}(J) + \mathcal{P}^{(2)}(J). \tag{34}$$

The SCF probability is then obtained from Eq. (33), by subtracting $\mathcal{P}^{\text{DCF}}(J)$ and the ICF probabilities of Eqs. (30) and (31). In this way, one gets Eq. (32) multiplied by a factor 2. However, as argued above, Eq. (33) double counts the contribution from SCF. To fix it, we start from Eqs. (30)–(32). Then, as it is done in experiments, one obtains the TF summing the contributions from the three fusion processes. In this way,

one gets

$$\mathcal{P}^{\rm TF}(J) = \mathcal{P}^{\rm DCF}(J) + \mathcal{P}^{\rm SCF}(J) + \mathcal{P}^{\rm ICF1}(J) + \mathcal{P}^{\rm ICF2}(J)$$
$$= \mathcal{P}^{\rm DCF}(J) + \mathcal{P}^{(1)}(J) + \mathcal{P}^{(2)}(J) - \mathcal{P}^{(1)}(J) \times \mathcal{P}^{(2)}(J).$$

The above expression does not double count SCF.

The theoretical cross sections for the different fusion processes are then given by

$$\sigma_{\rm SCF} = \frac{\pi}{K^2} \sum_J (2J+1)\, \mathcal{P}^{\rm SCF}(J), \tag{35}$$

$$\sigma_{\rm ICF1} = \frac{\pi}{K^2} \sum_J (2J+1)\, \mathcal{P}^{\rm ICF1}(J), \tag{36}$$

$$\sigma_{\rm ICF2} = \frac{\pi}{K^2} \sum_J (2J+1)\, \mathcal{P}^{\rm ICF2}(J), \tag{37}$$

and the observable CF, ICF, and TF cross sections are

$$\sigma_{\rm CF} = \sigma_{\rm DCF} + \sigma_{\rm SCF}, \tag{38}$$

$$\sigma_{\rm ICF} = \sigma_{\rm ICF1} + \sigma_{\rm ICF2}, \tag{39}$$

$$\sigma_{\rm TF} = \sigma_{\rm CF} + \sigma_{\rm ICF}. \tag{40}$$

We point out that our new expression for the SCF probability [Eq. (32)] does not contain the factor 2, included in the ^{7}Li fusion calculations of Refs. [48,49]. One then wonders how the results of those works would be affected by the removal of this factor. The contribution from SCF to the CF cross section strongly depends on the breakup threshold. In collisions of ^{7}Li ($B = 2.45$ MeV) at above-barrier energies it is responsible for $\approx$10% of the CF cross section, whereas at sub-barrier energies SCF is negligible. Then, the removal of the factor 2 would not lead to appreciable changes in the fusion cross sections of Refs. [48,49].

In collisions of ^{6}Li ($B = 1.47$ MeV) at above-barrier energies, the contributions from DCF and SCF are of the same order. On the other hand, SCF is negligible below the Coulomb barrier. Thus, in the case of ^{6}Li, removing factor 2 leads to an appreciable reduction of the CF cross section above the barrier. However, we point out that the spectroscopic amplitude also influences the cross sections. This amplitude is expected to be of the order of 1 (something between 0.5 and 1.0), but its precise value is not known. Then, we used it as a free parameter, varying it within this range. In this way, changes arising from the absence of factor 2 can be partly compensated by changing the spectroscopic amplitude.

III. APPLICATION: ^{6}Li COLLISIONS WITH HEAVY TARGETS

Now we use the theory of the previous sections to study CF and ICF in collisions of ^{6}Li projectiles with the heavy targets ^{124}Sn, ^{197}Au, ^{198}Pt, and ^{209}Bi. To determine the cross sections, we evaluate the probabilities $\mathcal{P}^{(1)}(J)$, $\mathcal{P}^{(2)}(J)$, and $\mathcal{P}^{\rm (DCF)}(J)$, given in the Appendix of Ref. [49]. The numerical calculations were performed by the code CF-ICF (unpublished), using intrinsic and radial wave functions obtained running the CDCC version of the FRESCO code [75].

The real part of the projectile-target interaction is given by Eq. (15), with $\mathbb{V}^{(i)}(r_i)$ $(i = 1, 2)$ given by the SPP between fragment c_i and the target.

For the imaginary potential, we adopted the prescription of Sec. II A 3. In the elastic channel (the only bound channel for ^{6}Li) we take the potential $\mathbb{W}_{PT}(R)$ of Eq. (19), with the parameters: $W_0 = 50$ MeV, $r_w = 1.0$ fm, and $a_w = 0.2$ fm. They are not exactly the same as in Ref. [47], but they lead to very similar results [76]. For the continuum-discretized space, we used the imaginary potential of Eq. (20), with $\mathbb{W}^{(1)}(r_1)$ and $\mathbb{W}^{(2)}(r_2)$ given by Woods-Saxon functions with parameters $W_0 = 50$ MeV, $r_w = 1.0$ fm, and $a_w = 0.2$ fm.

All calculations were performed with the spectroscopic amplitude [see Eqs. (16) and (18)] $\alpha = 0.7$, which leads to the best overall description of the data.

A. CF cross sections

Figure 5 shows the theoretical CF cross sections for collisions of ^{6}Li with ^{124}Sn [Figs. 5(a) and 5(b)], ^{197}Au [Figs. 5(c) and 5(d)], ^{198}Pt [Figs. 5(e) and 5(f)], and ^{209}Bi [Figs. 5(g) and 5(h)], in comparison with the data of Refs. [11,12,21,25,77].

The overall agreement between theory and experiment is excellent. It is particularly good at sub-barrier energies, even well below the Coulomb barrier, where the cross sections are as low as 10^{-4} mb. This means that collective excitations of the target do not play an important role in the reaction dynamics, and that the SPP is a suitable potential to represent the real part of the optical potential. Above the Coulomb barrier, the agreement is also very good, except for the ^{6}Li + ^{209}Bi system at the three data points with the highest energies, where the theoretical cross section falls slightly below the data.

Nowadays, it is well established that CF data on weakly bound systems at above-barrier energies are suppressed in comparison to predictions of barrier penetration models. The same conclusion is reached when one compares reduced CF data on weakly bound systems with those on tightly bound ones. However, the reaction mechanism responsible for the suppression is still under discussion [48,49,52,56,78]. In this discussion, the treatment of the continuum plays a central role. In our CDCC calculations, the continuum is approximated by bins formed by scattering states of the two fragments of the projectile. In Refs. [52,56], the fragment captured by the target is dominantly in an unbound state. Thus, neither of the projectile's fragments is bound to the target. Therefore, the space spanned by such states is the same as the breakup space of the CDCC calculation. The difference between the approaches of Refs. [52,56] and of Refs. [48,49] is that they use different bases to describe the continuum. As a matter of fact, a more realistic basis for the continuum would be the two-center molecular states adopted by Moschini and Diaz-Torres [79]. However, quantum mechanical calculations using this basis are very difficult to implement.

B. ICF and TF cross sections

Figure 6 shows ICF and TF cross sections calculated by our method, in comparison to the available data. The systems are the same as in Fig. 5. Inspecting the figure, one concludes

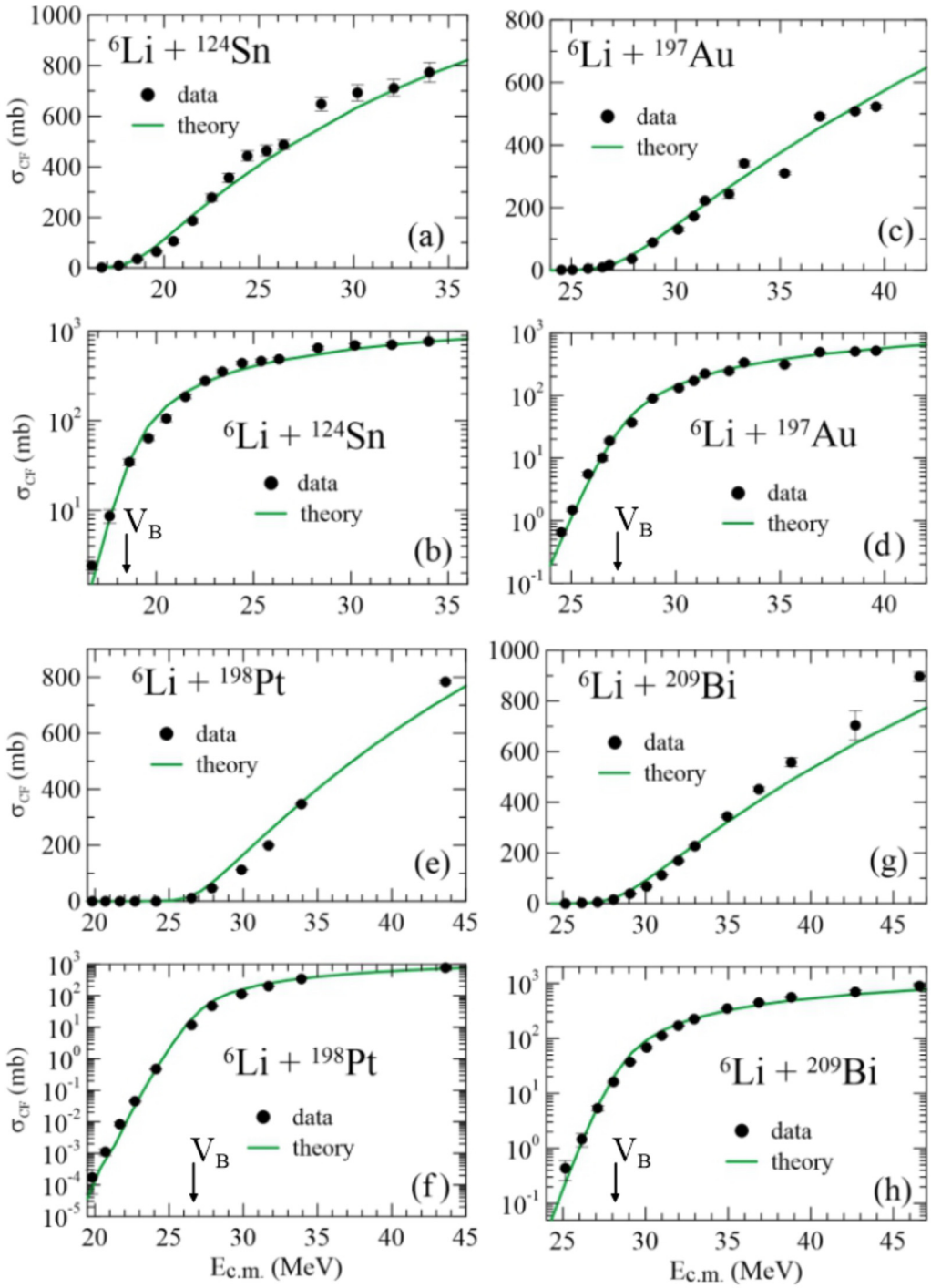

FIG. 5. Theoretical CF cross section in collisions of ^{6}Li with several heavy targets. The cross sections calculated by our model are compared with the data of Refs. [77] (^{6}Li + ^{124}Sn), [25] (^{6}Li + ^{197}Au), [21] (^{6}Li + ^{198}Pt), and [11,12] (^{6}Li + ^{209}Bi).

that the overall agreement between theory and experiment is reasonably good. A detailed discussion of each system is presented below.

The ICF and TF cross sections for the ^{6}Li + ^{124}Sn system are shown in Figs. 6(a) (linear scale) and 6(b) (logarithmic scale). First, we notice that the theoretical ICF and TF cross sections are essentially the same at energies well below the Coulomb barrier. The reason is that in this region the fusion cross section is completely dominated by ICF$_d$. Owing to its low mass, the transmission coefficient for this cluster to reach the strong absorption region is much larger than those for the heavier α cluster or the whole projectile.

The theoretical cross sections are compared with the data of Parkar *et al.* [77], obtained by on-line and off-line γ-ray detection techniques. The authors measured ICF$_d$ and ICF$_\alpha$ cross sections for several collision energies, but in two different experiments. Then, the beam energies were not always the same. In this way, the ICF cross section (sum of ICF$_d$ and

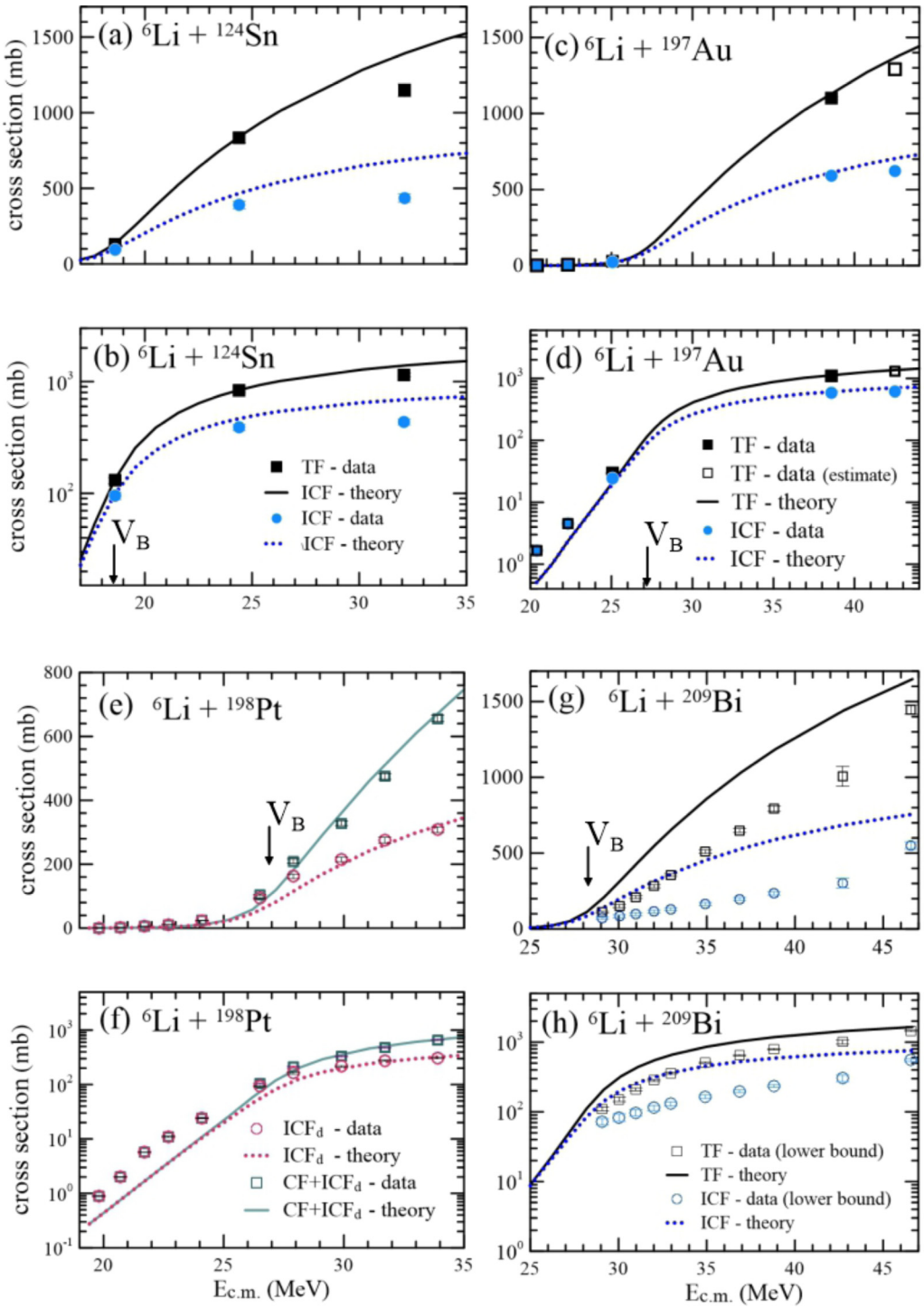

FIG. 6. Same as the previous figure but for TF and ICF cross sections. The data were extracted from the same references of the previous figure.

ICF_α) was not available at energies where only one of the ICF processes has been measured. For this reason, only three data points could be included in Fig. 6. The agreement between theory and experiment is good at the two lowest energies, but the theoretical prediction at the highest energy is larger than the experimental values.

The ICF and TF cross sections for the $^{6}\mathrm{Li} + {}^{197}\mathrm{Au}$ are shown in Figs. 6(c) and 6(d). The cross sections calculated by our model are compared to the data of Palshetkar *et al.* [25], obtained by on-line and off-line γ-ray detection techniques. As in the case of $^{6}\mathrm{Li} + {}^{124}\mathrm{Sn}$, the ICF_d and ICF_α cross sections were determined in two different experiments. Then, the figure includes only experimental cross sections at energies where both ICF_d and ICF_α cross sections have been measured. The agreement between theory and experiment is very good, except for the two data points with the lowest energies.

At these energies the theory underestimates the data. As we will show later in this section, this discrepancy arises from deuteron transfer, which is a reaction mechanism neglected in our calculations.

Now we consider the $^6\mathrm{Li} + {}^{198}\mathrm{Pt}$ system. Theoretical cross sections obtained by our model are shown in Figs. 6(e) and 6(f), in comparison to experimental cross sections of Shrivastava *et al.* [21]. The data were obtained in a highly sensitive experiment using off-beam γ-ray detection techniques, which allowed measurements of cross sections well below the Coulomb barrier. However, this experiment could measure only CF and ICF$_d$ cross sections. The isotopes formed by α capture followed by neutron evaporation deexcite exclusively by prompt γ-ray emission, which cannot be detected off-line. For this reason, the figure shows cross sections (both theoretical and experimental) for ICF$_d$ and CF + ICF$_d$, instead of ICF and TF. The agreement between theory and experiment is excellent, except at sub-barrier energies. As for the ^{197}Au target, this can be traced back to deuteron transfer (see the next sub-section).

Finally, we discuss ICF and TF for the $^6\mathrm{Li} + {}^{209}\mathrm{Bi}$ system. The theoretical cross sections are compared to the data of Dasgupta *et al.* [11,12], obtained by detection of the alpha particles emitted by the evaporation residues of the compound nuclei. Clearly, the theoretical cross sections are systematically higher than their experimental counterparts. However, the ICF and TF data are only lower bounds to the actual data. The reason is that the experiment misses the contribution from the ^{209}Po isotope, which could not be measured owing to its very long half-life (≈200 yr). According to statistical model estimates [12], this contribution is expected to be important at all beam energies of the experiment.

1. ICF$_d$ *vs direct transfer reactions*

In the experiment of Palshetkar *et al.* [25], the ICF$_d$ cross section for the $^6\mathrm{Li} + {}^{197}\mathrm{Au}$ system was determined through the detection of the γ rays emitted in the deexcitation of the Hg isotopes, produced by ICF$_d$ followed by neutron evaporation. However, these isotopes could also be formed by stripping reactions, where a proton or a deuteron is transferred to the target. A similar situation occurs in the measurements of the ICF$_d$ cross section for the $^6\mathrm{Li} + {}^{198}\mathrm{Pt}$ system, performed by Shrivastava *et al.* [21]. In this case, ICF$_d$ leads to ^{200}Au and lighter gold isotopes (after evaporation of neutrons), and these isotopes can also be formed by stripping reactions. The contribution from stripping reactions to the experimental ICF$_d$ cross section, which are not taken into account in our calculations, might be responsible for low ICF cross sections predicted by our model at sub-barrier energies, in comparison to the data.

To access the contribution of p and d stripping to the data of the $^6\mathrm{Li} + {}^{198}\mathrm{Pt}$ and $^6\mathrm{Li} + {}^{197}\mathrm{Au}$ systems, we evaluated the cross sections for these two processes, performing coupled reaction channel (CRC) calculations using the FRESCO code [75,80]. The calculations were performed in the prior representation, with complex remnants and the nonorthogonality terms. Since the sole purpose of these calculations was to provide an estimate of these stripping cross sections, we set all spectroscopic amplitudes equal to 1.

In the calculations of p transfer, the initial state was modeled by a valence proton orbiting around a ^{5}He core. Its wave function was obtained by solving the Schrödinger equation for a state with the experimental spin and parity, in a WS potential with depth fitted to reproduce the separation energy of the p within ^{6}Li. In the final partition, we considered the 27 states with lowest energies in the spectrum of the $(p + T)$ nucleus (T standing for target), and followed a similar procedure. Each intrinsic wave function was approximated by the solution of the Schrödinger equation for a WS potential, with the experimental spin and parity, and the depth of the potential was fitted to reproduce the experimental energy.

In the calculations of d transfer, the initial state was the same one used in our CDCC calculations of breakup and fusion cross sections. In the final partition, we adopted the extreme cluster model for the states of the $(d + T)$ nucleus, and followed a similar procedure. We considered the 14 states with lowest energies, and approximated them by cluster states with the same spin and parity, where the deuteron interacted with the target through a WS potential. The depth of this potential was fitted to reproduce the experimental excitation energy.

In our CRC calculations, we adopted the São Paulo potential [61,62] to represent the real part of the optical potentials in all partitions, and assumed that their imaginary parts had the same radial dependence. In this way, the optical potentials could be written as

$$U(R) = [1 + \lambda i] V(R). \tag{41}$$

For the final partition, we adopted the strength parameter $\lambda = 0.78$, which was successfully used to describe elastic scattering and total reaction cross sections in optical model calculations [81,82]. For the initial partition, we used a weaker imaginary potential, since the incident flux lost to transfer channels was explicitly taken into account in the CRC calculations. Then, we set $\lambda = 0.60$. This approach has been used in two-neutron transfer [83–89], two-proton transfer [88], and alpha-transfer [90] calculations, that described the data quite well.

Following the procedures described above, we performed CRC calculations of p- and d-stripping cross sections for the $^6\mathrm{Li} + {}^{197}\mathrm{Au}$ and the $^6\mathrm{Li} + {}^{198}\mathrm{Pt}$ systems. The results turned out to be extremely small. For both systems they were at least three orders of magnitude lower than the ICF$_d$ cross section of our model. Therefore, they cannot be responsible for the large discrepancies between the predictions of our model and the data at sub-barrier energies.

However, there is still one reaction mechanism that might give a relevant contribution to the measured d-capture cross section: the sequential stripping of a deuteron. In this process, a valence neutron is transferred to the target, giving rise to the intermediate partition $[^5\mathrm{Li}, (n + T)]$, and then a valence proton is stripped from the projectile, leading to the final partition, $[^4\mathrm{He}, (d + T)]$. Despite being a second order process, it may have a larger cross section than those of the two previously discussed first order processes. This could happen owing to the combination of two factors. First, the neutron-transfer probability tends to be large, since it is not hindered by a Coulomb barrier. Second, the kinematic

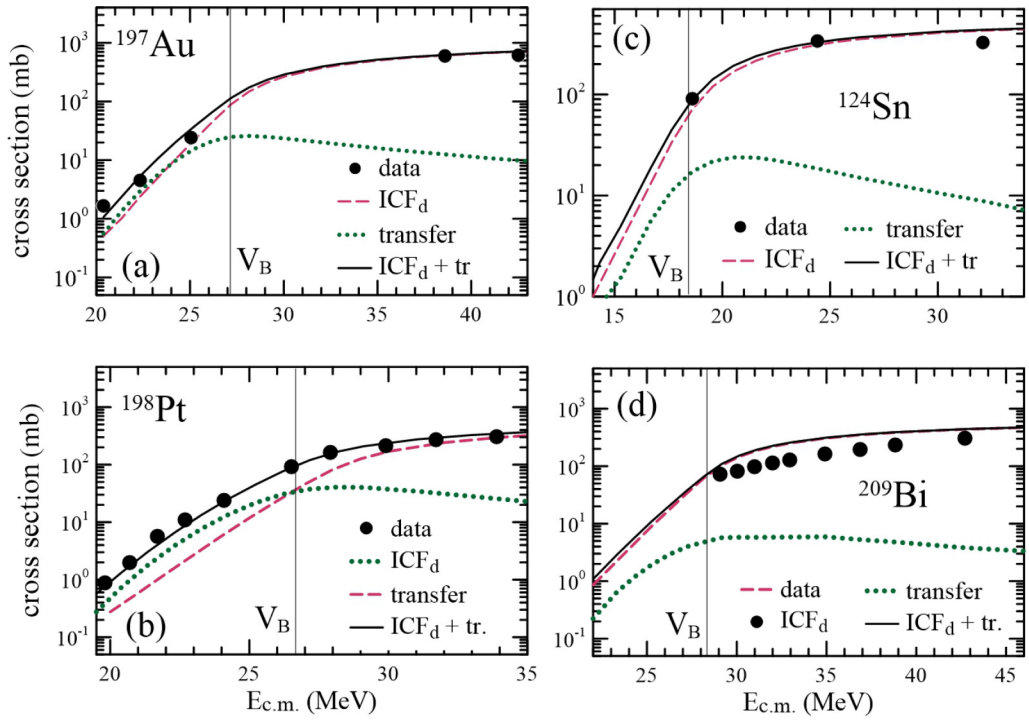

FIG. 7. d-capture cross sections for the collisions of ^{6}Li with (a) ^{197}Au, (b) ^{198}Pt, (c) ^{124}Sn, and (d) ^{124}Sn targets. The figure shows theoretical ICF$_d$ and sequential d-transfer cross sections, as well as the sum of the two (the d-capture cross section), in comparison to the data of Refs. [11,12,21,25,77]. For each system, the sub-barrier and above-barrier regions are separated by a thin vertical line. See the text for details.

conditions for proton transfer in the intermediate partition are much more favorable than in the initial partition. For the ^{6}Li + ^{197}Au system, the Q value for the direct stripping of a proton is 2.67 MeV, whereas the Q value for the transition from the intermediate partition ([^{5}Li, ^{198}Au]) to the final partition ([^{4}He, ^{199}Hg]) is 9.22 MeV. This difference is of great importance, since it is well known that cross sections for transfer of a charged particle are strongly enhanced by a high Q value [91,92]. The situation for the ^{6}Li + ^{198}Pt system is very similar. In this case, the corresponding Q values are 2.045 and 9.11 MeV. To check the importance of the above discussed process, we performed CRC calculations of d-transfer cross sections for the ^{6}Li + ^{197}Au and ^{6}Li + ^{198}Pt systems. In the intermediate partition, we considered states of the $(n + T)$ nucleus with excitation energies up to 1 MeV. To keep the numerical calculations feasible, the number of states in the final partition was reduced to 14. The imaginary part of the optical potential in the intermediate partition was given by Eq. (41), with $\lambda = 0.78$.

Figure 7 shows results of our calculations for the ^{6}Li + ^{197}Au [Fig. 7(a)] and ^{6}Li + ^{198}Pt [Fig. 7(b)] systems. The green dotted lines and the red dashed lines are the theoretical cross sections for sequential d transfer and for ICF$_d$, respectively. The black solid line is the sum of the two, representing an estimate of the d-capture cross section. Since the experiments cannot distinguish the two reaction mechanisms, the data should be compared to the black solid line. However, we should have in mind that this sum is just a rough estimate of what would be obtained in a realistic calculation involving breakup and transfer channels simultaneously (which could not be performed with the available computer resources). The situations for the two systems are very similar. At energies well below the Coulomb barrier, the d-transfer cross section is very important, and when it is added to the ICF$_d$ cross section the theoretical predictions are consistent with the data. On the other hand, the importance of the contribution from this process to the theoretical d-capture cross section decreases with the collision energy, becoming irrelevant above the Coulomb barrier. Thus, it is very likely that the difference between the predicted ICF cross section and the low-energy data arises from stripping reactions that contribute to the measured cross sections.

The above discussion of contributions from transfer processes to the measured d-capture cross section was based on the ^{6}Li + ^{197}Au and ^{6}Li + ^{198}Pt systems, where our model underestimates the data at sub-barrier energies. However, transfer processes could also contribute to the d-capture cross sections of the ^{6}Li + ^{124}Sn and ^{6}Li + ^{209}Bi systems. To check this possibility, we carried out similar CRC calculations for these systems. As for the ^{6}Li + ^{197}Au and ^{6}Li + ^{198}Pt reactions, the p transfer and the d transfer were found to be extremely small. The contribution from sequential d transfer starting by proton transfer was also negligible. The reasons were the same as explained above for the ^{6}Li + ^{197}Au and ^{6}Li + ^{198}Pt systems. Then, the only relevant process was the sequential d transfer consisting of a n transfer followed by a p transfer.

Figure 7 shows results of our calculations for the ^{6}Li + ^{124}Sn [Fig. 7(c)] and ^{6}Li + ^{209}Bi [Fig. 7(d)] systems. One observes that the d-transfer cross sections are very

small above the Coulomb barrier (the region at the right-hand side of the thin vertical lines), where the experimental data were measured. In fact, the d-transfer cross section is smaller than the ICF$_d$ cross section even at sub-barrier energies. This is quite different from the situation for the ^{6}Li + ^{197}Au and ^{6}Li + ^{198}Pt systems, where there are data at sub-barrier energies and the d-transfer cross section becomes larger than the ICF$_d$ cross sections in this energy region. These differences illustrate the strong dependence of transfer processes on the nuclear structure of the collision partners.

C. ICF$_d$ and ICF$_\alpha$ components of $\sigma_{\rm ICF}$

Now we calculate the individual contributions from the ICF$_d$ and ICF$_\alpha$ processes to the ICF cross section, and compare the predictions of our model to the available data. In fact, this kind of data is scarce for the systems studied in this paper. They are available only for the ^{6}Li + ^{124}Sn and ^{6}Li + ^{197}Au systems. As mentioned in the previous section, the ICF$_\alpha$ cross section for ^{6}Li + ^{198}Pt could not be measured by the off-line γ-ray technique used in the experiment of Shrivastava *et al.* [21]. The situation was still worse in the experiment of Dasgupta *et al.* [11,12], for the ^{6}Li + ^{209}Bi system. In this case, ICF$_\alpha$ and ICF$_d$ give rise to ^{213}At and ^{211}Po, respectively. These isotopes evaporate neutrons and deexcite by α decay. Detecting these α particles and identifying the emitter through their energies and half-lives, it would be possible to measure cross sections for the ICF process. However, the decay chains of ^{213}At and ^{211}Po get mixed at ^{210}At, as this isotope decays by the emission of β^+, leading to ^{210}Po. Then, the experiment cannot distinguish ICF$_d$ from ICF$_\alpha$. For this reason, the experiment of Refs. [11,12] did not report individual ICF$_d$ and ICF$_\alpha$ cross sections.

Figure 8 shows the predictions of our model for $\sigma_{\rm ICF_d}$ (green solid lines) and $\sigma_{\rm ICF_\alpha}$ (purple dashed lines) for the systems studied in this paper. The available data are also shown. Results for the ^{6}Li + ^{124}Sn system are shown in Figs. 8(a) and 8(b). The predictions of our theory are not in good agreement with the data of Parkar *et al.* [77]. Although the ICF$_d$ data points are not far from the theoretical curve, the theoretical ICF$_\alpha$ cross section is much larger than the data, at all collision energies. Qualitatively, the overall trend of the two ICF processes predicted by our model is consistent with the data. The ratio

$$\mathcal{R}_{\alpha/d} = \frac{\sigma_{\rm ICF_\alpha}}{\sigma_{\rm ICF_d}}$$

is less than 1 in the whole energy range. However, the theoretical prediction for this ratio is much larger than the one indicated by trends of the data.

Theoretical d-capture and ICF$_\alpha$ cross sections for the ^{6}Li + ^{197}Au system are compared to the data of Palshetkar *et al.* [25] in Figs. 8(c) and 8(d). In this case, the agreement between theory and experiment is much worse. Although the data points at some particular energies are close to the corresponding theoretical curve, the general trends of the calculated d-capture and ICF$_\alpha$ cross sections are very different from the experimental ones. As it happened for the ^{6}Li + ^{124}Sn system, our model predicts $\mathcal{R}_{\alpha/d} < 1$ at all collision energies, whereas the ratio of the two experimental cross sections is less than 1 at sub-barrier energies but it is larger than 1 above the Coulomb barrier [see dotted lines in Figs. 8(c) and 8(d)].

Results for the ^{6}Li + ^{198}Pt and ^{6}Li + ^{209}Bi systems are shown in Figs. 8(e)–8(h). One finds that the theoretical d-capture cross section for the former system is in excellent agreement with the data, as already shown in the previous figure. We could not compare the remaining theoretical cross section to the experiment, since no further ICF data are available for these systems. However, one can observe that the general trends of the theoretical curves for the two systems are the same. In both cases $\mathcal{R}_{\alpha/d} < 1$ in the whole energy interval of our calculations.

The overall trend of the theoretical ICF cross sections can be better understood if the ratio $\mathcal{R}_{\alpha/d}(x)$ is plotted against the dimensionless energy variable of the fusion function reduction method [8,9]:

$$x = \frac{E - V_B^{00}}{\hbar\omega^{00}}. \tag{42}$$

Above, V_B^{00} and $\hbar\omega^{00}$ are the barrier parameters of $V_{00}(R)$, given in Table III. This is done in Fig. 9, for the ^{6}Li + ^{124}Sn, ^{6}Li + ^{197}Au, ^{6}Li + ^{198}Pt, and ^{6}Li + ^{209}Bi systems. One concludes that, according to our model, this ratio has a very weak dependence on the target. However, one should keep in mind that this conclusion is valid for one particular weakly bound projectile (^{6}Li), colliding with heavy targets within a limited mass interval ($124 < A_T < 209$). Further, one notices that this ratio grows consistently with the collision energy, with a slight oscillation in the neighborhood of $x = 0$. For $-1 < x < 4$, it varies in the range [0.1, 0.6].

IV. CONCLUSIONS

We have presented a refined version of a recently proposed method [48,49] to calculate cross sections for the fusion processes taking place in collisions of weakly bound nuclei. Improving the treatment of the direct absorption of the whole projectile by the target, we eliminated the overestimation of the CF cross section at sub-barrier energies. Further, we have emphasized the difference between cross sections calculated by the CDCC method and the ones measured in actual experiments. The procedures to evaluate CF and ICF cross sections using results of CDCC calculations were then rediscussed. The method was used to evaluate CF and ICF cross sections in collisions of ^{6}Li projectiles with ^{124}Sn, ^{197}Au, ^{198}Pt, and ^{209}Bi targets, and our results were compared to the available data.

The overall agreement between the calculated CF cross sections and the data was excellent, in the whole energy range of the calculations. An important point is that the agreement is equally good at energies well below the Coulomb barrier, where our previous calculations for ^{7}Li overestimated the data [49]. Note that the targets considered in our calculations do not have collective states that would enhance sub-barrier fusion. Since SCF is negligible in this energy range, the good agreement between theory and experiment is an indication

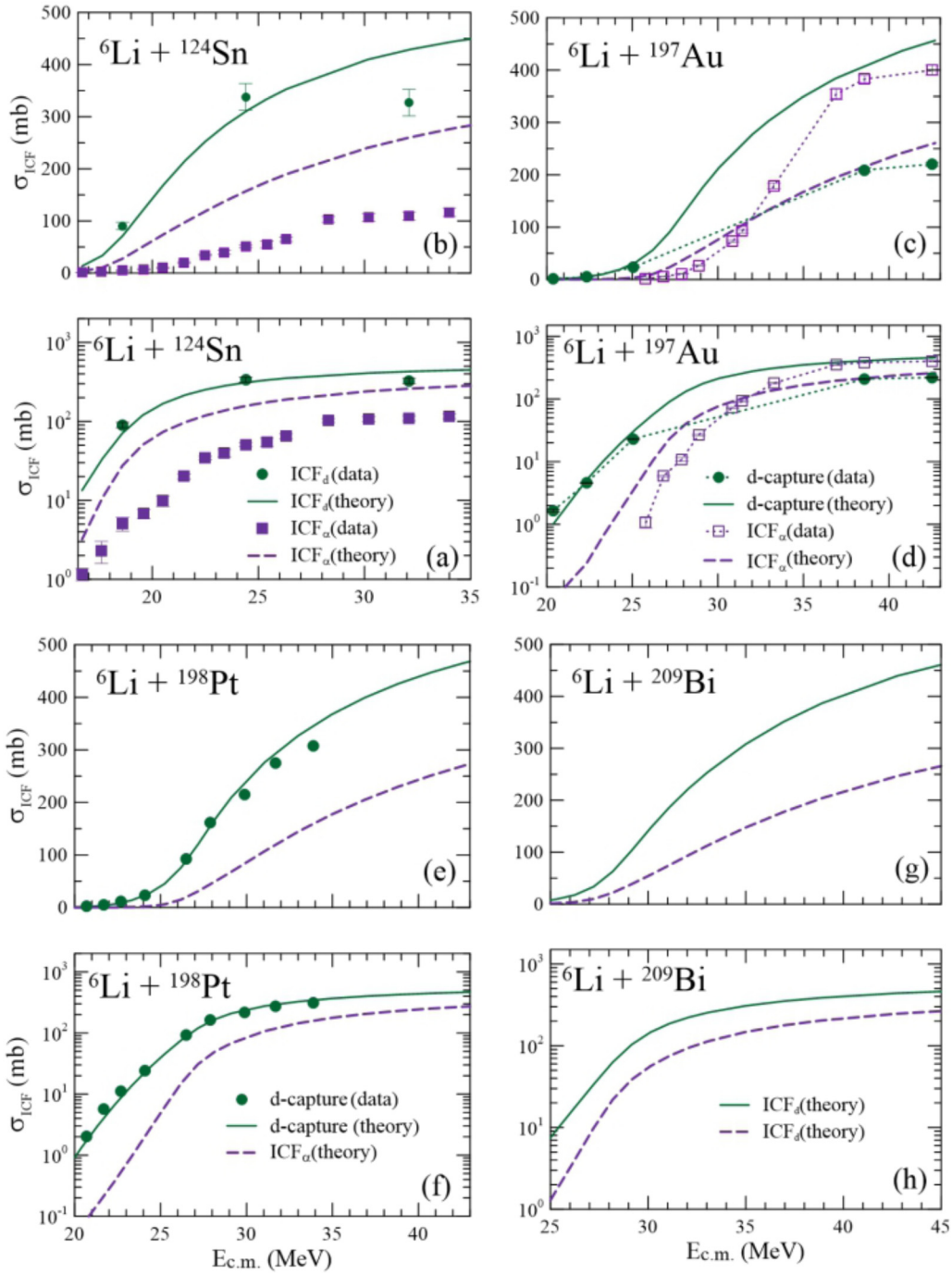

FIG. 8. Theoretical and experimental ICF$_d$ and ICF$_\alpha$ cross sections in collisions of ^{6}Li with ^{124}Sn, ^{197}Au, ^{198}Pt, and ^{209}Bi targets. The data are from Refs. [11,12,21,25,77]. In the cases of ^{197}Au and ^{198}Pt, σ_{ICF_d} is replaced by the d-capture cross section, which includes also the contribution from the sequential d transfer.

that the São Paulo potential leads to a realistic Coulomb barrier.

The ICF and TF cross sections calculated by our model were in reasonable agreement with the data, except for the data points of the ^{6}Li + ^{197}Au and ^{6}Li + ^{198}Pt systems at energies well below the Coulomb barrier. In these cases, our model underpredicted the experimental cross sections. However, we have shown that these discrepancies can be traced back to contributions from sequential strippings of the projectile, which lead to the same nucleus as in the ICF$_d$ process. We remark that ICF data for the systems studied in the present paper are scarce in the literature. In collisions with ^{198}Pt, only the ICF$_d$ cross section has been measured, and in the case of ^{209}Bi only lower bounds to the ICF cross section have been reported.

We have investigated also the contributions from the ICF$_d$ and ICF$_\alpha$ processes to the ICF cross sections. We concluded that the theoretical ICF$_d$ cross section is systematically higher

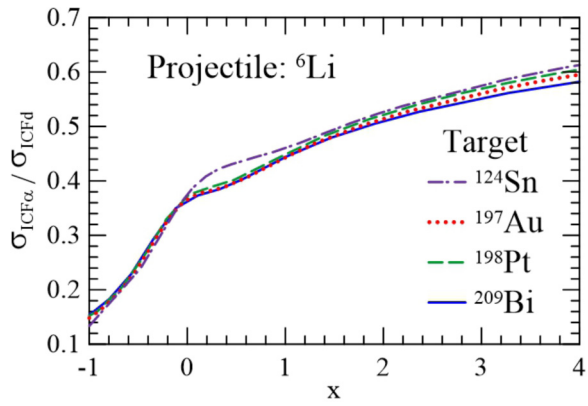

FIG. 9. Ratios of theoretical cross sections for the two ICF processes as functions of the reduced collision energy [8,9], for the ^{6}Li + ^{124}Sn, ^{6}Li + ^{197}Au, ^{6}Li + ^{198}Pt, and ^{6}Li + ^{209}Bi systems.

than the ICF$_\alpha$ one. The ratio $\mathcal{R}_{\alpha/d} = \sigma_{\mathrm{ICF}_\alpha}/\sigma_{\mathrm{ICF}_d}$ varies between 0.1 and 0.6, growing monotonically with the collision energy. Further, our model predicted that the dependence of this ratio on the target is very weak, at least for the heavy targets in the mass range considered in this paper. In this regard, the predictions of our model are not consistent with the data. The experimental ratio for ^{124}Sn grows monotonically with E but it is much smaller than the one obtained in our calculations. In the case of ^{197}Au, the experimental ratio is below 1 at sub-barrier energies, but it grows very rapidly with E, becoming larger than 1 at $E \approx 30$ MeV. We believe that these discrepancies call for further investigations.

ACKNOWLEDGMENTS

Work was supported in part by the Brazilian funding agencies CNPq, FAPERJ, CAPES, and INCT-FNA (Instituto Nacional de Ciência e Tecnologia, Física Nuclear e Aplicações), research Project No. 464898/2014-5. We are indebted to Prof. Raul Donangelo for critically reading the paper.

[1] L. F. Canto, P. R. S. Gomes, R. Donangelo, and M. S. Hussein, Phys. Rep. **424**, 1 (2006).
[2] N. Keeley, R. Raabe, N. Alamanos, and J. L. Sida, Prog. Part. Nucl. Phys. **59**, 579 (2007).
[3] N. Keeley, N. Alamanos, K. W. Kemper, and K. Rusek, Prog. Part. Nucl. Phys. **63**, 396 (2009).
[4] L. F. Canto, P. R. S. Gomes, R. Donangelo, J. Lubian, and M. S. Hussein, Phys. Rep. **596**, 1 (2015).
[5] J. J. Kolata, V. Guimarães, and E. F. Aguilera, Eur. Phys. J. A **52**, 123 (2016).
[6] P. R. S. Gomes, D. R. Mendes Junior, L. F. Canto, J. Lubian, and P. N. de Faria, Few-Body Syst. **57**, 205 (2016).
[7] L. Canto, V. Guimarães, J. Lubian, and M. Hussein, Eur. Phys. J. A **56**, 281 (2020).
[8] L. F. Canto, P. R. S. Gomes, J. Lubian, L. C. Chamon, and E. Crema, J. Phys. G **36**, 015109 (2009).
[9] L. F. Canto, P. R. S. Gomes, J. Lubian, L. C. Chamon, and E. Crema, Nucl. Phys. A **821**, 51 (2009).
[10] L. F. Canto, D. R. Mendes, Jr., P. R. S. Gomes, and J. Lubian, Phys. Rev. C **92**, 014626 (2015).
[11] M. Dasgupta, D. J. Hinde, K. Hagino, S. B. Moraes, P. R. S. Gomes, R. M. Anjos, R. D. Butt, A. C. Berriman, N. Carlin, C. R. Morton, J. O. Newton, and A. Szanto de Toledo, Phys. Rev. C **66**, 041602(R) (2002).
[12] M. Dasgupta, P. R. S. Gomes, D. J. Hinde, S. B. Moraes, R. M. Anjos, A. C. Berriman, R. D. Butt, N. Carlin, J. Lubian, C. R. Morton, J. O. Newton, and A. Szanto de Toledo, Phys. Rev. C **70**, 024606 (2004).
[13] A. Mukherjee, S. Roy, M. K. Pradhan, M. S. Sarkar, P. Basu, B. Dasmahapatra, T. Bhattacharya, S. Bhatacharya, S. K. Basu, A. Chatterjee *et al.*, Phys. Lett. B **636**, 91 (2006).
[14] R. Broda, M. Ishihara, B. Herskind, H. Oeschler, S. Ogaza, and H. Ryde, Nucl. Phys. A **248**, 356 (1975).
[15] M. K. Pradhan, A. Mukherjee, P. Basu, A. Goswami, R. Kshetri, R. Palit, V. V. Parkar, M. Ray, S. Roy, P. R. Chowdhury, M. S. Sarkar, and S. Santra, Phys. Rev. C **83**, 064606 (2011).
[16] P. K. Rath, S. Santra, N. L. Singh, B. K. Nayak, K. Mahata, R. Palit, K. Ramachandran, S. K. Pandit, A. Parihari, A. Pal, S. Appannababu, S. K. Sharma, D. Patel, and S. Kailas, Phys. Rev. C **88**, 044617 (2013).
[17] P. K. Rath, S. Santra, N. L. Singh, R. Tripathi, V. V. Parkar, B. K. Nayak, K. Mahata, R. Palit, S. Kumar, S. Mukherjee, S. Appannababu, and R. K. Choudhury, Phys. Rev. C **79**, 051601(R) (2009).
[18] P. K. Rath, S. Santra, N. L. Singh, K. Mahata, R. Palit, B. K. Nayak, K. Ramachandran, V. V. Parkar, R. Tripathi, S. K. Pandit *et al.*, Nucl. Phys. A **874**, 14 (2012).
[19] I. J. Thompson, M. A. Nagarajan, J. A. Lilley, and M. J. Smithson, Nucl. Phys. A **505**, 84 (1989).
[20] A. Shrivastava, A. Navin, A. Diaz-Torres, V. Nanal, K. Ramachandran, M. Rejmund, S. Bhattacharyya, A. Chatterjee, S. Kailas, A. Lemasson *et al.*, Phys. Lett. B **718**, 931 (2013).
[21] A. Shrivastava, A. Navin, A. Lemasson, K. Ramachandran, V. Nanal, M. Rejmund, K. Hagino, T. Ichikawa, S. Bhattacharyya, A. Chatterjee, S. Kailas, K. Mahata, V. V. Parkar, R. G. Pillay, and P. C. Rout, Phys. Rev. Lett. **103**, 232702 (2009).
[22] C. L. Guo, G. L. Zhang, S. P. Hu, J. C. Yang, H. Q. Zhang, P. R. S. Gomes, J. Lubian, X. G. Wu, J. Zhong, C. Y. He, Y. Zheng, C. B. Li, G. S. Li, W. W. Qu, F. Wang, L. Zheng, L. Yu, Q. M. Chen, P. W. Luo, H. W. Li, Y. H. Wu, W. K. Zhou, B. J. Zhu, and H. B. Sun, Phys. Rev. C **92**, 014615 (2015).
[23] H. Kumawat, V. Jha, V. V. Parkar, B. J. Roy, S. K. Pandit, R. Palit, P. K. Rath, C. F. Palshetkar, S. K. Sharma, S. Thakur, A. K. Mohanty, A. Chatterjee, and S. Kailas, Phys. Rev. C **86**, 024607 (2012).
[24] V. V. Parkar, S. K. Sharma, R. Palit, S. Upadhyaya, A. Shrivastava, S. K. Pandit, K. Mahata, V. Jha, S. Santra, K. Ramachandran, T. N. Nag, P. K. Rath, B. Kanagalekar, and T. Trivedi, Phys. Rev. C **97**, 014607 (2018).
[25] C. F. Palshetkar, S. Thakur, V. Nanal, A. Shrivastava, N. Dokania, V. Singh, V. V. Parkar, P. C. Rout, R. Palit, R. G. Pillay, S. Bhattacharyya, A. Chatterjee, S. Santra, K.

Ramachandran, and S. L. Singh, Phys. Rev. C **89**, 024607 (2014).
[26] M. Dasgupta, D. J. Hinde, R. D. Butt, R. M. Anjos, A. C. Berriman, N. Carlin, P. R. S. Gomes, C. R. Morton, J. O. Newton, A. Szanto de Toledo, and K. Hagino, Phys. Rev. Lett. **82**, 1395 (1999).
[27] C. S. Palshetkar, S. Santra, A. Chatterjee, K. Ramachandran, S. Thakur, S. K. Pandit, K. Mahata, A. Shrivastava, V. V. Parkar, and V. Nanal, Phys. Rev. C **82**, 044608 (2010).
[28] P. R. S. Gomes, I. Padrón, E. Crema, O. A. Capurro, J. O. F. Niello, G. V. Martí, A. Arazi, M. Trotta, J. Lubian, M. E. Ortega *et al.*, Phys. Lett. B **634**, 356 (2006).
[29] P. R. S. Gomes, I. Padron, E. Crema, O. A. Capurro, J. O. FernandezNiello, A. Arazi, G. V. Marti, J. Lubian, M. Trotta, A. J. Pacheco, J. E. Testoni, M. D. Rodriguez, M. E. Ortega, L. C. Chamon, R. M. Anjos, R. Veiga, M. Dasgupta, D. J. Hinde, and K. Hagino, Phys. Rev. C **73**, 064606 (2006).
[30] Y. D. Fang, P. R. S. Gomes, J. Lubian, X. H. Zhou, Y. H. Zhang, J. L. Han, M. L. Liu, Y. Zheng, S. Guo, J. G. Wang, Y. H. Qiang, Z. G. Wang, X. G. Wu, C. Y. He, Y. Zheng, C. B. Li, S. P. Hu, and S. H. Yao, Phys. Rev. C **87**, 024604 (2013).
[31] Y. D. Fang, P. R. S. Gomes, J. Lubian, M. L. Liu, X. H. Zhou, D. R. MendesJunior, N. T. Zhang, Y. H. Zhang, G. S. Li, J. G. Wang, S. Guo, Y. H. Qiang, B. S. Gao, Y. Zheng, X. G. Lei, and Z. G. Wang, Phys. Rev. C **91**, 014608 (2015).
[32] N. T. Zhang, Y. D. Fang, P. R. S. Gomes, J. Lubian, M. L. Liu, X. H. Zhou, G. S. Li, J. G. Wang, S. Guo, Y. H. Qiang, Y. H. Zhang, D. R. MendesJunior, Y. Zheng, X. G. Lei, B. S. Gao, Z. G. Wang, K. L. Wang, and X. F. He, Phys. Rev. C **90**, 024621 (2014).
[33] M. Dasgupta, D. J. Hinde, S. L. Sheehy, and B. Bouriquet, Phys. Rev. C **81**, 024608 (2010).
[34] G. S. Li, J. G. Wang, J. Lubian, H. O. Soler, Y. D. Fang, M. L. Liu, N. T. Zhang, X. H. Zhou, Y. H. Zhang, B. S. Gao, Y. H. Qiang, S. Guo, S. C. Wang, K. L. Wang, K. K. Zheng, R. Li, and Y. Zheng, Phys. Rev. C **100**, 054601 (2019).
[35] F. Gollan, D. Abriola, A. Arazi, M. A. Cardona, E. de Barbará, J. de Jesús, D. Hojman, R. M. I. Betan, J. Lubian, A. J. Pacheco, B. Paes, D. Schneider, and H. O. Soler, Phys. Rev. C **104**, 024609 (2021).
[36] M. Kaushik, G. Gupta, S. Thakur, H. Krishnamoorthy, P. P. Singh, V. V. Parkar, V. Nanal, A. Shrivastava, R. G. Pillay, K. Mahata, K. Ramachandran, S. Pal, C. S. Palshetkar, and S. K. Pandit, Phys. Rev. C **101**, 034611 (2020).
[37] K. Hagino, M. Dasgupta, and D. J. Hinde, Nucl. Phys. A **738**, 475 (2004).
[38] A. Diaz-Torres, D. J. Hinde, J. A. Tostevin, M. Dasgupta, and L. R. Gasques, Phys. Rev. Lett. **98**, 152701 (2007).
[39] A. Diaz-Torres, J. Phys. G **37**, 075109 (2010).
[40] A. Diaz-Torres, Comput. Phys. Commun. **182**, 1100 (2011).
[41] H. D. Marta, L. F. Canto, and R. Donangelo, Phys. Rev. C **89**, 034625 (2014).
[42] G. D. Kolinger, L. F. Canto, R. Donangelo, and S. R. Souza, Phys. Rev. C **98**, 044604 (2018).
[43] N. Keeley, K. W. Kemper, and K. Rusek, Phys. Rev. C **65**, 014601 (2001).
[44] A. Diaz-Torres, I. J. Thompson, and C. Beck, Phys. Rev. C **68**, 044607 (2003).
[45] P. Descouvemont, T. Druet, L. F. Canto, and M. S. Hussein, Phys. Rev. C **91**, 024606 (2015).
[46] K. Hagino, A. Vitturi, C. H. Dasso, and S. M. Lenzi, Phys. Rev. C **61**, 037602 (2000).
[47] A. Diaz-Torres and I. J. Thompson, Phys. Rev. C **65**, 024606 (2002).
[48] J. Rangel, M. Cortes, J. Lubian, and L. F. Canto, Phys. Lett. B **803**, 135337 (2020).
[49] M. R. Cortes, J. Rangel, J. L. Ferreira, J. Lubian, and L. F. Canto, Phys. Rev. C **102**, 064628 (2020).
[50] S. Hashimoto, K. Ogata, S. Chiba, and M. Yahiro, Prog. Theor. Phys. **122**, 1291 (2009).
[51] V. V. Parkar, V. Jha, and S. Kailas, Phys. Rev. C **94**, 024609 (2016).
[52] J. Lei and A. M. Moro, Phys. Rev. Lett. **122**, 042503 (2019).
[53] M. Ichimura, N. Austern, and C. M. Vincent, Phys. Rev. C **32**, 431 (1985).
[54] M. Boselli and A. Diaz-Torres, J. Phys. G **41**, 094001 (2014).
[55] M. Boselli and A. Diaz-Torres, Phys. Rev. C **92**, 044610 (2015).
[56] K. J. Cook, E. C. Simpson, L. T. Bezzina, M. Dasgupta, D. J. Hinde, K. Banerjee, A. C. Berriman, and C. Sengupta, Phys. Rev. Lett. **122**, 102501 (2019).
[57] J. Lei and A. M. Moro, Phys. Rev. Lett. **123**, 232501 (2019).
[58] Y. Sakuragi, M. Yahiro, and M. Kamimura, Prog. Theor. Phys. Suppl. **89**, 136 (1986).
[59] N. Austern, Y. Iseri, M. Kamimura, M. Kawai, G. Rawitscher, and M. Yashiro, Phys. Rep. **154**, 125 (1987).
[60] L. F. Canto and M. S. Hussein, *Scattering Theory of Molecules, Atoms and Nuclei* (World Scientific, Singapore, 2013).
[61] L. C. Chamon, D. Pereira, M. S. Hussein, M. A. Candido Ribeiro, and D. Galetti, Phys. Rev. Lett. **79**, 5218 (1997).
[62] L. C. Chamon, B. V. Carlson, L. R. Gasques, D. Pereira, C. De Conti, M. A. G. Alvarez, M. S. Hussein, M. A. Cândido Ribeiro, E. S. Rossi, Jr., and C. P. Silva, Phys. Rev. C **66**, 014610 (2002).
[63] D. H. Luong, M. Dasgupta, D. J. Hinde, R. du Rietz, R. Rafieri, C. J. Lin, M. Evers, and A. Diaz-Torres, Phys. Lett. B **695**, 105 (2011).
[64] G. L. Zhang, G. X. Zhang, S. P. Hu, Y. J. Yao, J. B. Xiang, H. Q. Zhang, J. Lubian, J. L. Ferreira, B. Paes, E. N. Cardozo, H. B. Sun, J. J. Valiente-Dobon, D. Testov, A. Goasduff, P. R. John, M. Siciliano, F. Galtarossa, R. Francesco, D. Mengoni, D. Bazzacco, E. T. Li, X. Hao, and W. W. Qu, Phys. Rev. C **97**, 014611 (2018).
[65] N. Arena, S. Cavallaro, A. D'Arrigo, G. Fazio, G. Giardina, A. Italiano, and A. Taccone, J. Phys. G **16**, 1511 (1990).
[66] C. M. Castaneda, H. A. Smith, P. P. Singh, and H. Karwowski, Phys. Rev. C **21**, 179 (1980).
[67] W. von Ortzen and A. Vitturi, Rep. Prog. Phys. **64**, 1247 (2001).
[68] S. Kahana and A. J. Baltz, *Advances in Nuclear Physics* (Plenum, New York, 1977), Vol. 9, p. 1.
[69] R. A. Broglia, O. Hansen, and C. Riedel, *Advances in Nuclear Physics* (Plenum, New York, 1973), Vol. 6, p. 287.
[70] N. Anyas-Weiss, J. C. Cornell, P. S. Fisher, P. N. Hudson, A. Menchaca-Rocha, D. J. Millener, A. D. Panagiotou, D. K. Scott, D. Strottman, D. M. Brink *et al.*, Phys. Rep. **12**, 201 (1974).
[71] H. F. Zhang and G. Royer, Phys. Rev. C **77**, 054318 (2008).
[72] S. Guo, X. Bao, Y. Gao, J. Li, and H. Zhang, Nucl. Phys. A **934**, 110 (2015).
[73] H. Feshbach, Ann. Phys. (NY) **19**, 287 (1962); **5**, 357 (1958).
[74] L. F. Canto, B. V. Carlson, and R. Donangelo, Braz. J. Phys. **51**, 181 (2021).
[75] I. J. Thompson, Comput. Phys. Rep. **7**, 167 (1988).

[76] L. F. Canto, R. Donangelo, M. S. Hussein, P. Lotti, J. Lubian, and J. Rangel, Phys. Rev. C **98**, 044617 (2018).
[77] V. V. Parkar, S. K. Pandit, A. Shrivastava, R. Palit, K. Mahata, V. Jha, K. Ramachandran, S. Gupta, S. Santra, S. K. Sharma, S. Upadhyaya, T. N. Nag, S. Bhattacharya, T. Trivedi, and S. Kailas, Phys. Rev. C **98**, 014601 (2018).
[78] S. K. Pandit, A. A. Shrivastava, K. Mahata, N. Keeley, V. V. Parkar, R. Palit, P. C. Routa, K. Ramachandrana, A. Kumar, S. Bhattacharyya *et al.*, Phys. Lett. B **820**, 136570 (2021).
[79] L. Moschini and A. Diaz-Torres, Phys. Lett. B **820**, 136513 (2021).
[80] http://www.fresco.org.uk.
[81] D. Sousa, D. Pereira, J. Lubian, L. Chamon, J. Oliveira, E. Rossi, C. Silva, P. de Faria, V. Guimarães, R. Lichtenthaler *et al.*, Nucl. Phys. A **836**, 1 (2010).
[82] L. R. Gasques, L. C. Chamon, P. R. S. Gomes, and J. Lubian, Nucl. Phys. A **764**, 135 (2006).
[83] D. Carbone, J. L. Ferreira, F. Cappuzzello, J. Lubian, C. Agodi, M. Cavallaro, A. Foti, A. Gargano, S. M. Lenzi, R. Linares, and G. Santagati, Phys. Rev. C **95**, 034603 (2017).
[84] E. N. Cardozo, J. Lubian, R. Linares, F. Cappuzzello, D. Carbone, M. Cavallaro, J. L. Ferreira, A. Gargano, B. Paes, and G. Santagati, Phys. Rev. C **97**, 064611 (2018).
[85] R. Linares, M. J. Ermamatov, J. Lubian, F. Cappuzzello, D. Carbone, E. N. Cardozo, M. Cavallaro, J. L. Ferreira, A. Foti, A. Gargano, B. Paes, G. Santagati, and V. A. B. Zagatto, Phys. Rev. C **98**, 054615 (2018).
[86] B. Paes, G. Santagati, R. M. Vsevolodovna, F. Cappuzzello, D. Carbone, E. N. Cardozo, M. Cavallaro, H. Garcia-Tecocoatzi, A. Gargano, J. L. Ferreira, S. M. Lenzi, R. Linares, E. Santopinto, A. Vitturi, and J. Lubian, Phys. Rev. C **96**, 044612 (2017).
[87] M. J. Ermamatov, R. Linares, J. Lubian, J. L. Ferreira, F. Cappuzzello, D. Carbone, M. Cavallaro, M. Cubero, P. N. de Faria, A. Foti, G. Santagati, and V. A. B. Zagatto, Phys. Rev. C **96**, 044603 (2017).
[88] D. Carbone, J. L. Ferreira, S. Calabrese, F. Cappuzzello, M. Cavallaro, A. Hacisalihoglu, H. Lenske, J. Lubian, R. I. MagnanaVsevolodovna, E. Santopinto, C. Agodi, L. Acosta, D. Bonanno, T. Borello-Lewin, I. Boztosun, G. A. Brischetto, S. Burrello, D. Calvo, E. R. ChavezLomeli, I. Ciraldo, M. Colonna, F. Delaunay, N. Deshmukh, P. Finocchiaro, M. Fisichella, A. Foti, G. Gallo, F. Iazzi, L. LaFauci, G. Lanzalone, R. Linares, N. H. Medina, M. Moralles, J. R. B. Oliveira, A. Pakou, L. Pandola, H. Petrascu, F. Pinna, S. Reito, G. Russo, O. Sgouros, S. O. Solakci, V. Soukeras, G. Souliotis, A. Spatafora, D. Torresi, S. Tudisco, A. Yildirin, and V. A. B. Zagatto, Phys. Rev. C **102**, 044606 (2020).
[89] U. Umbelino, K. C. C. Pires, R. Lichtenthaler, V. Scarduelli, G. A. Scotton, A. Lepine-Szily, V. Guimaraes, J. Lubian, B. Paes, J. L. Ferreira, M. A. G. Alvarez, J. M. B. Shorto, S. Appannababu, M. Assuncao, R. P. Condori, and V. Morcelle, Phys. Rev. C **99**, 064617 (2019).
[90] J. L. Ferreira, J. Lubian, R. Linares, M. J. Ermamatov, H. Yepez-Martinez, and P. O. Hess, Eur. Phys. J. A **55**, 94 (2019).
[91] W. Von Oertzen, H. Bohlen, and B. Gebauer, Nucl. Phys. A **207**, 91 (1973).
[92] F. D. B. P. R. Christensen, V. I. Manko, and R. J. Nickles, Nucl. Phys. A **207**, 33 (1973).